Chemical-Looping Combustion Process: Kinetics and Mathematical Modeling

Ion Iliuta, Raul Tahoces, and Gregory S. Patience
Dept. of Chemical Engineering - École Polytechnique de Montreal, Canada H3C 3A7

Sebastien Rifflart and Francis Luck
TOTAL S.A. - Place de la Coupole, 92078 Paris La Défense Cedex, France

DOI 10.1002/aic.11967
Published online January 6, 2010 in Wiley InterScience (www.interscience.wiley.com).

Chemical Looping Combustion technology involves circulating a metal oxide between a fuel zone where methane reacts under anaerobic conditions to produce a concentrated stream of CO_2 and water and an oxygen rich environment where the metal is reoxidized. Although the needs for electrical power generation drive the process to high temperatures, lower temperatures (600–800°C) are sufficient for industrial processes such as refineries. In this paper, we investigate the transient kinetics of NiO carriers in the temperature range of 600 to 900°C in both a fixed bed microreactor (WHSV = 2-4 g CH_4/h/g oxygen carrier) and a fluid bed reactor (WHSV = 0.014-0.14 g CH_4/h per g oxygen carrier). Complete methane conversion is achieved in the fluid bed for several minutes. In the microreactor, the methane conversion reaches a maximum after an initial induction period of less than 10 s. Both CO_2 and H_2O yields are highest during this induction period. As the oxygen is consumed, methane conversion drops and both CO and H_2 yields increase, whereas the CO_2 and H_2O concentrations decrease. The kinetics parameter of the gas–solids reactions (reduction of NiO with CH_4, H_2, and CO) together with catalytic reactions (methane reforming, methanation, shift, and gasification) were estimated using experimental data obtained on the fixed bed microreactor. Then, the kinetic expressions were combined with a detailed hydrodynamic model to successfully simulate the comportment of the fluidized bed reactor.
© 2010 American Institute of Chemical Engineers *AIChE J,* 56: 1063–1079, 2010
Keywords: combustion, fluidization, reaction kinetics, reactor analysis

Introduction

Combustion of fossil fuels for power generation emits a significant amount of CO_2 to the atmosphere. It is generally accepted that reduction in greenhouse gas emissions is necessary to avoid major climatic changes.[1] In recent years, chemical-looping combustion (CLC), proposed by Ritcher and Knoche,[2] has received growing interest as an efficient and low-cost combustion technology for the selective capture of CO_2 and the substantial reduction of NO_x emissions from fossil fuel-based power generation stations. This nonconventional technique is a two-step process that necessitates a system composed of two reactors, an air (regeneration) and a fuel (reducing) reactor, and an oxygen carrier circulating between the reactors that transfer the oxygen necessary for the fuel combustion.

The key issue in the CLC system's performance is the oxygen carrier—typically a metal oxide. Iron, nickel, and copper have been selected as the most promising metals to be used in a CLC process. Oxides of these metals supported on several inert binders have been found to react with

Correspondence concerning this article should be addressed to I. Iliuta at Ion.iliuta@gch.ulval.ca
Current Address of I. Iliuta: Dept. of Chemical Engineering, Laval University, Québec, Canada G1K 7P4.

© 2010 American Institute of Chemical Engineers

sufficiently high rates during successive reduction–oxidation cycles. Besides high reactivity, the oxygen carriers must be resistant to attrition, fluidizable with little tendency to form agglomerates at high temperature.[3] Recently, Wolf et al.[4] carried out a comparative study regarding system energy efficiency with Fe- and Ni-based oxygen carriers and found that CLC Ni-based carriers were technically superior compared with other metal oxides. Mattisson et al.[5,6] compared the behavior of Fe-, Ni-, Cu-, and Mn-based oxygen carriers prepared by freeze granulation in a fluidized bed reactor and observed that oxygen carriers based on Ni or Cu showed the highest reactivity. They found agglomeration problems working with some Fe-based oxygen carriers and especially working with Cu-based oxygen carriers. Copeland et al.[7] eliminated Cu as a potential oxygen carrier due to agglomeration problems in the fluidized bed facility and obtained successfully results with Fe- and Ni-based carriers. On the other hand, de Diego et al.[8] prepared by impregnation CuO/Al_2O_3 oxygen carriers, which did not present agglomeration problems. These oxygen carriers had high oxygen transport capacity and achieved complete CH_4 combustion to CO_2 and H_2O. However, due to the low melting point of Cu (1063°C), low temperatures are recommended. The superior reactivity, thermal stability, negligible volatility of Ni-based oxygen carrier constitutes favorable factors for CLC and the objective of this work was to join the advantages of Ni–O and to study the reaction kinetics based on original experimental data collected in both a microfixed bed reactor and a fluidized bed reactor in the temperatures range of 600 to 900°C.

There are remarkable differences between CLC with respect to conventional combustion processes. In this latter case, the flue gas is comprised of a dilute stream of CO_2 in N_2; in which case, energy intensive and costly separation technology would be required to concentrate the CO_2 for subsequent sequestration. In the case of CLC, there are two exhaust streams: one from the air reactor that is predominantly of N_2 and residual O_2 (and Ar)and the other one from the fuel reactor that contains CO_2 and H_2O. Consequently, CO_2 is delivered without any extra energy penalty for disposal.[9]

From a technological standpoint, the regeneration of the metal to the metal oxide is highly exothermic and design allowances must be considered to account for the possibility of high-temperature excursions to avoid thermal sintering of the carrier. In practice, fluidized bed reactors are ideally suited to maintain isothermal operation. Additionally, the reduction stage is endothermic for most inorganic oxides (CuO being one exception). Overall, the CLC process must be well designed to couple the air and fuel reactors efficiently. Lyngfelt et al.[10] implemented CLC in two interconnected fluidized bed reactors (the air and fuel reactor) with the oxygen carrier circulating between the units. Methane is introduced to the fuel reactor, which contains an oxygen carrier that is reduced according to the global reaction:

$$(2n+m)\mathrm{Me}_x\mathrm{O}_y + \mathrm{C}_n\mathrm{H}_{2m} \rightarrow (2n+m)\mathrm{Me}_x\mathrm{O}_{y-1} + n\mathrm{CO}_2 + m\mathrm{H}_2\mathrm{O}$$

where Me_xO_y is the fully oxidized oxygen carrier and Me_xO_{y-1} is the reduced oxygen carrier. This reaction corresponds to the complete oxidation of the fuel, which is important to ensure to avoid dilution of the CO_2 by unconverted fuel or incomplete combustion products such as CO and H_2. At the exit of the fuel reactor, the oxygen carrier is reduced to Me_xO_{y-1} and reoxided by air in the regenerator:

$$2\mathrm{Me}_x\mathrm{O}_{y-1} + \mathrm{O}_2 \rightarrow 2\mathrm{Me}_x\mathrm{O}_y$$

The oxidized oxygen carrier, Me_xO_y, is then transported back to the fuel reactor for another cycle. A schematic of the process is presented in Figure 1.

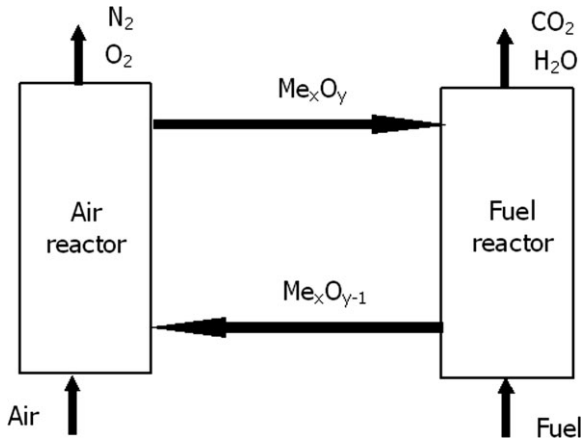

Figure 1. Chemical looping combustion process.

Although reactor design, modeling, and hydrodynamics have been elaborated by several research groups, these topics still require more attention.[1] It is clear that the need for rapid scale up and optimal commercialization of the fluidized bed systems for CLC necessitates an improved understanding and quantification of the fluid dynamics and the transport processes coupled with the complex chemistry and the thermodynamic and the thermal effects. Particularly, availability of engineering-type models for improved design and scale up, based on the observed physical phenomena, is desirable for one important reason: the computational fluid dynamics codes, based on the first principles, are yet insufficient to be effective tools for the design of commercial fluidized bed reactors. The reason for this inadequacy lies first in the complexity of the gas–solid flow in fluidized bed reactors, which makes the computations excessively time consuming and that the additional consideration of chemical-looping combustion reactions and particularly the handling of the necessarily large geometries of commercial reactors easily exceed the presently available computing capacities. In the interim period, it is essential to develop engineering models for the description of mixing and transport.

This work deals with the development of a chemical reaction engineering (CRE) model for the CLC in a fluidized bed reactor to evaluate the selectivity and conversion as well as the hydrodynamics of the fluid bed. We first establish a solid-state kinetic model of the reduction of Ni-based oxygen carrier particles by CH_4. The kinetics was estimated using the experimental data collected in a fixed bed microreactor under isothermal conditions. Then, we summarize the main steps for developing a simplified hydrodynamic platform that serves as a backbone for the CRE model. The CRE model consists of the so-called hydrodynamic platform on which will be grafted the CLC reactions.

Table 1. Physical Characterization of Support and Oxygen Carrier

Particles	Mercury volume (cm^3/g)	Surface area by BET, macro, meso and micropores (m^2/g)
Support (Al_2O_3)	0.189	187
Carrier ($NiO + Al_2O_3$)	0.172	102

Experimental Section

Oxygen carrier

The FCC catalyst Krystal 212 NP from Grace Davison (Deerfield, IL), with 47% Al_2O_3 and 48% SiO_2 was used as support to prepare the oxygen carrier by impregnation. The nickel nitrate solution was added dropwise to the powder such that its volume equaled the total pore volume (intra- and inter-) of the alumina. The mixture was stirred at room temperature followed by drying at 120°C for 12 h and calcination at 850°C in air for 5 h. The solids were sieved to a particle diameter of 140 μm. After this treatment, the powder contained 15wt% Ni. The surface area, measured by nitrogen BET (Autsorb-1 Quantachrome Instruments, Boynton Beach, FL), dropped from 187 to 102 m^2/g as shown in Table 1. The pore volume, measured by mercury intrusion (Poremaster 33, Quantachrome Instruments, Boynton Beach, FL) remained essentially constant at about 180 cm^3/g.

Two reactors were used to establish the reaction kinetics: a fixed bed microreactor that was run with 0.1 g of powder and fluidized bed reactor that was operated with solids inventories as much as 300 g.

Fixed bed microreactor

A general scheme of the experimental setup is shown in Figure 2. The microreactor was housed in an electrical furnace (Hiden Catlab, Hiden Analytical Inc., Livonia, MI) and the gas manifold was configured to minimize the cross-contamination of the methane and oxygen as well as to minimize the pressure perturbation while switching. The gases were metered to the reactor with Brooks mass flow controllers (MFC) (Brooks Instrument, Hatfield, PA). At all times during the cycling, argon went to either the vent or to the reactor. The cycle was initiated by feeding methane to the reactor and argon to the vent. After a specified period of time, which could reach up to 10 min (and more), the four-port valve was switched to purge the reactor of methane and reaction products for a period of 2 min. At the same time, the methane/argon MFC was switched off and the oxygen/argon MFC was turned on. The 2-min purge time allowed the oxygen/argon gases to flush out the feed line upstream of the four-port valve. The four-point valve was then switched allowing the air/argon mixture to proceed to the reactor and the argon stream went to the vent. To minimize the pressure perturbations caused by the valve switch, the pressure drop in the vent line at the four-port valve was set to approximately equal the pressure drop across the reactor (and the lines upstream and downstream). This configuration was controlled automatically and we were able to test the catalyst stability with over 2000 cycles between oxidation and reduction.

The fixed bed microreactor was made of quartz with a 4-mm internal diameter. The gas flow rate was 100 ml/min. The oxidizing gas consisted of 21 vol% oxygen in argon and the reducing gas was varied from 5 to 10 vol% of CH_4 in argon. We were also able to replace CH_4 by CO or H_2 in the reducing gas. Temperatures from 600 to 900°C were used. The effluent stream was sampled continually with a quadrupole mass spectrometer (Hiden) at a frequency as low as 0.3 s^{-1}. Under reducing conditions, the detected species were CH_4 as the reactant gas and CO_2, CO, H_2O, and H_2 as the reactions products. During the oxidation period, the detected species were O_2 as the reactant gas and CO and CO_2 as the reactions products from carbon deposit oxidation.

Fluidized bed reactor

Multicycle reduction–oxidation experiments were carried out in a quartz reaction with an inner diameter of 46 mm that increased to 70 mm at the exit, as shown in Figure 3. It was operated at the same pressure, temperature and methane concentration as the microreactor but the WHSV was lower: 0.014 −0.14 g CH_4/h/g oxygen carrier. As shown in Figure 4, the feed manifold system included two multipoint valves. The eight-port valve vented through a back pressure regulator and then to atmosphere or to the reactor. The four-port valve allowed a mixture of either methane/argon or argon to go to the reactor. The pressure drop in the lines was set to equal the pressure drop across the reactor to minimize pressure perturbations during valve switching. Switching between oxidizing, reducing, and inert environments was computer controlled and the effluent gases were monitored by the mass spectrometer. The flow rates of the argon and synthetic air (21% O_2 in Ar) were controlled by two Brooks MFCs with a maximum of 2000 ml/min STP. A third Brooks MFC metered the methane and it had a maximum rate of 1200 ml/min STP. The tests were generally carried out with 300 g of catalyst and a flow rate of 1000 and 2000 ml/min STP. The reducing gas composition contained between 10 and 50% methane in argon, whereas all reoxidation experiments were carried out with 21% O_2. As with the microreactor, an argon purge between the reduction step and oxidation step minimized the mixing of the two feed gases.

Two electrical band heaters, one placed in the fluidized bed section and the other placed in the disengagement section, maintained essentially isothermal conditions throughout

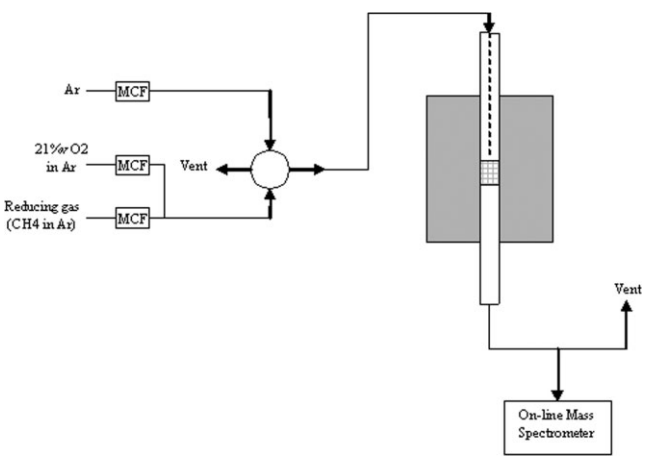

Figure 2. Fixed bed microreactor experimental setup.

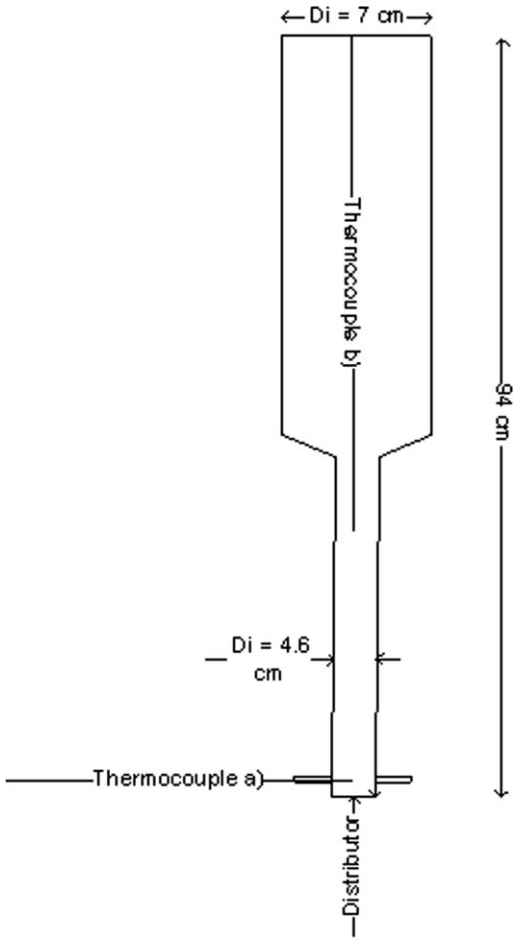

Figure 3. Fluidized bed reactor geometry.

the reactor. A multiport thermocouple was positioned in the centre to monitor the temperature. Most experiments were carried out at temperatures between 600 and 900°C.

Kinetic model

Reaction Mechanism. With Ni-based oxygen carriers prepared on Al_2O_3, high H_2, and CO concentrations were present in the outlet gas together with CO_2 and H_2O during the reduction period (Figure 5). To describe this behavior, we considered two options for methane oxidation to CO_2: (1) the direct reaction of CH_4 to CO_2, without CO as intermediate state (reaction 1), and (2) the complete methane oxidation to CO_2 with CO as an intermediate state in a two-step process (reactions 3 and 4):

(1) The curious feature of the methane breakthrough is that it increases initially, indicating low activity, and subsequently drops — high activity — before rising again. This would indicate that there is some activation process during the initial stages of methane contact. To account for this "activation" step, I have modified the reaction mechanism slightly and allow methane to react with NiO to produce H_2 and CO_2 directly (reaction 1), (without CO as intermediate state).

(2) On the other side, in fixed bed microreactor, the oxygen ratio, defined as the amount of oxygen that is reacting with the fuel in reduction period compared to what is needed for total combusting, was very low. These conditions favor the methane partial oxidation[11] and the reduction process is mainly selective toward the formation of H_2 and CO (reaction 4). In this case, the complete methane oxidation to CO_2 takes place through CO formation in a two-step process (reactions 3 and 4), (CO is an intermediate state).

The presence of H_2 simultaneously with water suggests that the complete methane oxidation to H_2O takes place through H_2 formation in a two-step process (reactions 1 and 2).

This behavior is similar with that found with Ni-based oxygen carriers prepared on γ- Al_2O_3 by Adanez et al.[12]:

$$CH_4 + 2NiO \leftrightarrow 2Ni + 2H_2 + CO_2 \quad (1)$$

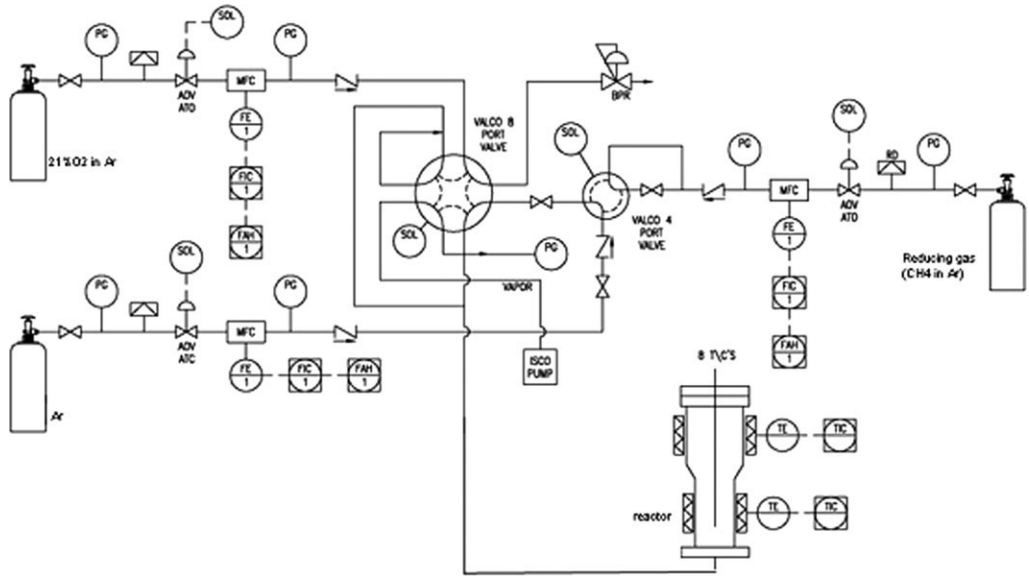

Figure 4. Fluidized bed reactor feed manifold system.

$$H_2 + NiO \leftrightarrow Ni + H_2O \quad (2)$$

$$CO + NiO \leftrightarrow Ni + CO_2 \quad (3)$$

$$CH_4 + NiO \leftrightarrow Ni + 2H_2 + CO \quad (4)$$

Radical reactions are probable for this system,[13,14] but treating them quantitatively was beyond the scope of this particular project. To closely approach physical reality of chemical- looping combustion process, future refinements of the model can be implemented to account for radical reactions via the methane combustion mechanism on NiO proposed by Dewaele and Froment.[13]

The Ni formed during reduction catalyzes both methane reforming (reactions 5 and 6) and especially CH_4 decomposition (reaction 7).[12,26] Methanation of carbon monoxide (reaction 8) and shift reaction (reaction 9) are two secondary reactions which could be highly significant.[12] A possible route for methane oxidation is reaction 7 followed by reactions 9 or 11.

$$CH_4 + H_2O \overset{Ni}{\leftrightarrow} CO + 3H_2 \quad (5)$$

$$CH_4 + CO_2 \overset{Ni}{\leftrightarrow} 2CO + 2H_2 \quad (6)$$

$$CH_4 + Ni \leftrightarrow Ni - C + 2H_2 \quad (7)$$

$$CO + 3H_2 \overset{Ni}{\leftrightarrow} CH_4 + H_2O \quad (8)$$

$$CO + H_2O \overset{Ni}{\leftrightarrow} CO_2 + H_2 \quad (9)$$

$$C + CO_2 \overset{Ni}{\leftrightarrow} 2CO \quad (10)$$

$$C + H_2O \overset{Ni}{\leftrightarrow} CO + H_2 \quad (11)$$

Noncatalytic gas–solid reactions kinetics

There are two types of models to describe noncatalytic gas–solid kinetics: structured-type (porous or grain) and volumetric models. The structured-type model explicitly consider the structural solid changes during reaction by modeling the variation of the internal solid matrix (grain models: Szekely et al.[15]; Heesink et al.[16]) or the internal pore structure (pore development models: Bhatia and Perlmutter[17,18]; Gavalas.[19,20]) In the volumetric-type approach, in contrast, the changes in pore structure during conversion are considered by using experimental correlations.

In this work two gas–solid reaction models, shrinking core and volumetric particle model were used to evaluate the noncatalytic gas–solid reduction kinetics (reactions 1–4).[21] It has been found that the reduction of NiO/Al_2O_3 particles can be represented by both the shrinking core and volumetric models. From the agreement between experimental data and both models, the volumetric particle model is a slightly better representation of the data and, for this reason, kinetics is based on this model.

A continuum description of the porous solid particle was assumed in the volumetric model. This supposition presumes that the largest length scale characteristic of the solid structure is much smaller than the characteristic length associated with the concentration gradients. The reaction rate per unit of oxygen carrier mass was formulated in a "structured" form. Thus, a function which summarizes the reaction sites available at a given time was introduced. To incorporate explicitly this feature, we assume the following intrinsic kinetics at any location within the particle:

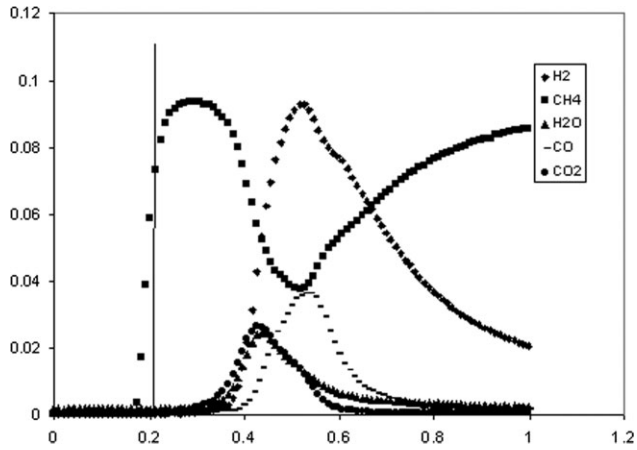

Figure 5. Experimental gas product distribution obtained during the reduction with CH_4 (10%) of Ni15-Al_2O_3 in fixed bed microreactor at 600°C (wet basis, u_{SG} = 0.424 m/s, NiO conversion = 0.88).

Time $t = 0$ indicates when the inert gas is switched to the reacting gas.

$$r_{mi} = a_0 S(X) r_{si} \quad (12)$$

The reaction rate has been split into two factors: the first factor, $S(X)$, takes into account the effect of the change of available reacting surface, whereas the second one embodies the effect of gas concentration on reaction rate. According to particle volumetric model,[22] the active surface area decreases linearly with the increase of conversion:

$$S(X) = 1 - X \quad (13)$$

The solid molar balance for the oxygen carrier and reduced oxygen carrier assuming that there is no influence of external and internal mass transfer on the reaction rate are:

$$\frac{dC'_{NiO}(\text{kmol/kg}_{\text{carrier}})}{dt} = -r_{NiO} = -\sum_i \nu_{NiO,i} r_{mi} \quad (14a)$$

$$\frac{dC'_{Ni}(\text{kmol/kg}_{\text{carrier}})}{dt} = r_{Ni} = \sum_i \nu_{Ni,i} r_{mi} \quad (14b)$$

In terms of oxygen carrier conversion, and considering the reactions are first order with respect to the concentration of reactant gas, the mole balance equation for oxygen carrier is:

$$\frac{dX}{dt} = \frac{a_0(1-X)}{C'^0_{NiO}} [(2k_{s1} + k_{s4}) C_{CH_4} C_{NiO} C_{Ni} + (k_{s2} C_{H_2} + k_{s3} C_{CO}) C_{NiO}] \quad (15)$$

There is some activation process during the initial stages of methane contact (Figure 5), which was taken in to

Table 2. Activation Energies and Pre-exponential Factors for the Final Model: Noncatalytic Gas–Solid Reactions

	E_1 (kJ/mol)	E_2 (kJ/mol)	E_3 (kJ/mol)	E_4 (kJ/mol)	$k_{1,0}$	$k_{2,0} \times 10^4$	$k_{3,0} \times 10^4$	$k_{4,0} \times 10^3$
Estimate	77.41	26.41	26.5	23.66	4.66	1.31	1.098	4.18
UL	77.55	33.05	29.04	25.37	4.59	3.08	1.48	5.31
LL	77.28	19.23	23.97	21.70	4.74	0.54	0.81	3.29

UL, upper limit; LL, lower limit of approximate 95% confidence interval.

account by the reaction of CH_4 with the surface site to produce hydrogen and carbon dioxide (reaction 1) and by the partial oxidation of CH_4 to hydrogen and carbon monoxide (reaction 4). There is also, an important modification to the kinetic rate expression for the reactions which involves methane (reactions 1 and 4): the rate is proportional to the concentration of methane, concentration of oxidized sites as well as the concentration of reduced sites. The last term is responsible for the good fit between the model and experimental data of the methane breakthrough curve.

The mass balance equations for NiO and Ni are as follows:

$$\frac{dC_{NiO}}{dt} = -a_0(1-X)[(2k_{s1}+k_{s4})C_{CH_4}C_{NiO}C_{Ni} + (k_{s2}C_{H_2}+k_{s3}C_{CO})C_{NiO}]M_{NiO} \quad (16)$$

$$\frac{dC_{Ni}}{dt} = a_0(1-X)[(2k_{s1}+k_{s4})C_{CH_4}C_{NiO}C_{Ni} + (k_{s2}C_{H_2}+k_{s3}C_{CO})C_{NiO}]M_{Ni} \quad (17)$$

The rate parameters of the noncatalytic gas–solid kinetics (k_{s1}, k_{s2}, k_{s3}, and k_{s4}) were obtained by means of nonlinear regression of the experimental data using Powell's algorithm:

$$k_{s1} = 4.66\exp(-77416/RT) \quad (18)$$

$$k_{s2} = 1.31 \times 10^{-4}\exp(-26413/RT) \quad (19)$$

$$k_{s3} = 1.097 \times 10^{-4}\exp(-26505/RT) \quad (20)$$

$$k_{s4} = 4.18 \times 10^{-3}\exp(-23666/RT) \quad (21)$$

The parameters were tested by their 95% confidence interval and by physicochemical criteria such as the Arrhenius law.[29] Table 2 shows the rate parameters of the noncatalytic gas–solid reactions and the approximate 95% confidence intervals. The parity diagram is shown in Figure 6a.

Catalytic gas–solid reactions kinetics

The kinetics of the catalytic gas–solid reactions was evaluated using representative models of the literature. Several reaction rate constants were re-evaluated under CLC conditions using the experimental data obtained in the fixed bed microreactor. The other reaction rate constants, the adsorption coefficients, and the thermodynamic equilibrium constants were taken from the original kinetic models.

The kinetic model developed by Hou and Houghes,[23] based on the mechanism that both methane and steam are adsorbed and dissociated on the catalyst and considering that the surface reactions between adsorbed species is rate controlling, was used to estimate the kinetics of water gas shift reaction and methane reforming with H_2O. The basic assumption of the definitive kinetic mechanism are: adsorption of H2O on the catalyst and dissociation, adsorption of CH_4 on the catalyst and dissociation, surface reaction with the formation of adsorbed CHO and H, adsorbed CHO dissociates to adsorbed CO and H or reacts with adsorbed oxygen yielding adsorbed CO2 and H in parallel (rate-determining step), desorption of CO, CO_2, and H_2. The intrinsic rate equations derived by using the Langmuir-Hinshelwood-Hougen-Watson (LHHW) approach and Freundlich's adsorption concept are the following:

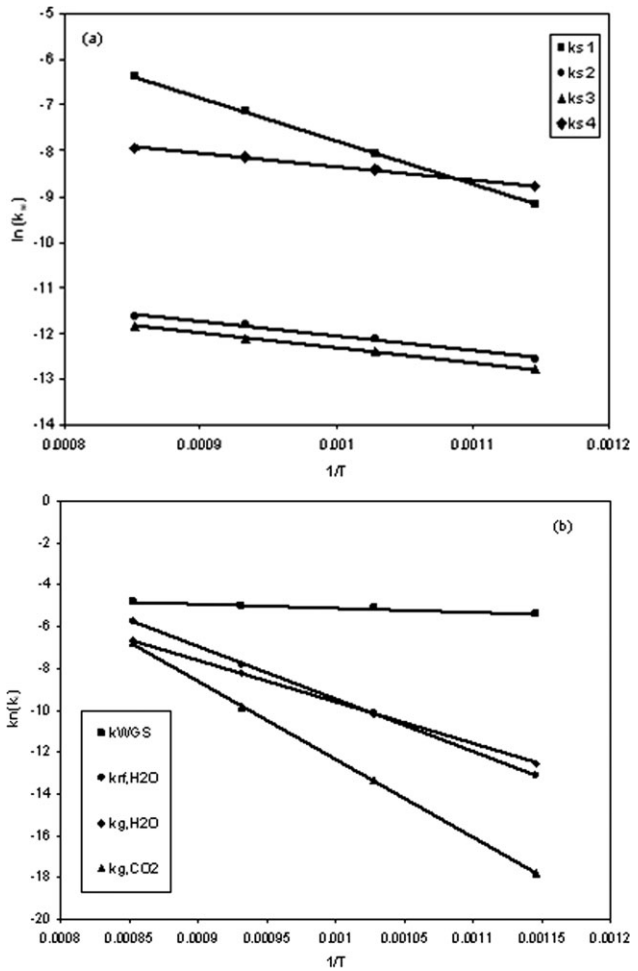

Figure 6. Temperature dependence of rate parameters of the noncatalytic (a) and catalytic (b) gas–solid reactions.

Points: values estimated by nonlinear regression; lines: calculated from values of Tables 2 and 3.

$$r_{\mathrm{rf,H_2O}} = \frac{k_{\mathrm{rf,H_2O}} \frac{p_{\mathrm{CH_4}} p_{\mathrm{H_2O}}^{0.5}}{p_{\mathrm{H_2}}^{1.25}} \left[1 - \frac{p_{\mathrm{CO}} p_{\mathrm{H_2}}^3}{K_{\mathrm{p,rf,H_2O}} p_{\mathrm{CH_4}} p_{\mathrm{H_2O}}}\right]}{\left(1 + K_{\mathrm{CO,rf,H_2O}} p_{\mathrm{CO}} + K_{\mathrm{H_2,rf,H_2O}} p_{\mathrm{H_2}}^{0.5} + K_{\mathrm{H_2O,rf,H_2O}} \frac{p_{\mathrm{H_2O}}}{p_{\mathrm{H_2}}}\right)^2} \quad (22)$$

$$r_{\mathrm{WGS}} = \frac{k_{\mathrm{WGS}} \frac{p_{\mathrm{CO}} p_{\mathrm{H_2O}}^{0.5}}{p_{\mathrm{H_2}}^{0.5}} \left[1 - \frac{p_{\mathrm{CO}} p_{\mathrm{H_2}}}{K_{\mathrm{p,WGS}} p_{\mathrm{CO}} p_{\mathrm{H_2O}}}\right]}{\left(1 + K_{\mathrm{CO,rf,H_2O}} p_{\mathrm{CO}} + K_{\mathrm{H_2,rf,H_2O}} p_{\mathrm{H_2}}^{0.5} + K_{\mathrm{H_2O,rf,H_2O}} \frac{p_{\mathrm{H_2O}}}{p_{\mathrm{H_2}}}\right)^2} \quad (23)$$

The adsorption coefficients of CO, H_2, H_2O, the equilibrium constants, and the reaction rate constants of reactions 5 and 9 are:

$$K_{\mathrm{CO,rf,H_2O}} = 5.18 \times 10^{-11} \exp(140000/\mathrm{RT}),\ \mathrm{bar}^{-1} \quad (24)$$

$$K_{\mathrm{H_2,ref,H_2O}} = 5.7 \times 10^{-9} \exp(93400/\mathrm{RT}),\ \mathrm{bar}^{-0.5} \quad (25)$$

$$K_{\mathrm{H_2O,rf,H_2O}} = 9.25 \exp(-15900/\mathrm{RT}) \quad (26)$$

$$K_{\mathrm{p,rf,H_2O}} = 1.17 \times 10^{13} \exp(-26830/\mathrm{T}),\ \mathrm{bar}^2 \quad (27)$$

$$K_{\mathrm{p,WGS}} = 1.77 \times 10^{-2} \exp(4400/\mathrm{T}) \quad (28)$$

$$k_{\mathrm{rf,H_2O}} = 6.237 \times 10^6 \exp(-209000/\mathrm{RT}),\ \mathrm{kmol}/(\mathrm{kg_{Ni}\ s\ bar^{0.25}}) \quad (29)$$

$$k_{\mathrm{WGS}} = 3.8 \times 10^{-2} \exp(-15400/\mathrm{RT}),\ \mathrm{kmol}/(\mathrm{kg_{Ni}\ s\ bar}) \quad (30)$$

The kinetic model developed by Wang and Lu,[24] based on the mechanism that both methane and CO_2 are adsorbed on the catalyst with the methane dissociation and considering that the surface reaction between adsorbed C and CO_2 is rate controlling, was used to estimate the kinetics of methane reforming with CO_2. The intrinsic rate equation derived using the Langmuir-Hinshelwood-Hougen-Watson (LHHW) approach and Freundlich's adsorption concept is the following:

$$r_{\mathrm{rf,CO_2}} = \frac{k_{\mathrm{rf,CO_2}} p_{\mathrm{CH_4}} p_{\mathrm{CO_2}}}{\left(1 + K_{\mathrm{CH_4,rf,CO_2}} p_{\mathrm{CH_4}}\right)\left(1 + K_{\mathrm{CO_2,rf,CO_2}} p_{\mathrm{CO_2}}\right)} \cong \frac{k_{\mathrm{rf,CO_2}} p_{\mathrm{CH_4}} p_{\mathrm{CO_2}}}{1 + K_{\mathrm{CO_2,rf,CO_2}} p_{\mathrm{CO_2}}} \quad (31)$$

The adsorption coefficient of CO_2 and the rate constant of methane reforming with CO_2 are:

$$k_{\mathrm{rf,CO_2}} = 0.207 \exp(-9920/\mathrm{RT}), \mathrm{kmol}/(\mathrm{kg_{Ni}\ s\ bar^2}) \quad (32)$$

$$K_{\mathrm{CO_2,rf,CO_2}} = 2.4 \times 10^{-3} \exp(77500/\mathrm{RT}),\ \mathrm{bar}^{-1} \quad (33)$$

The kinetics of the methanation of carbon monoxide was satisfactorily explained by assuming equilibrium of dissociative carbon monoxide and hydrogen adsorption and hydrogenation of surface carbon to a CH_2-species involving two adsorbed hydrogen atoms as the rate limiting step[25]:

$$r_{\mathrm{CH_4,m}} = \frac{k_{\mathrm{CH_4,m}} K_{\mathrm{CO,m}} K_{\mathrm{H_2,m}}^2 p_{\mathrm{CO}}^{0.5} p_{\mathrm{H_2}}}{\left(1 + K_{\mathrm{CO,m}} p_{\mathrm{Co}}^{0.5} + K_{\mathrm{H_2,m}} P_{\mathrm{H_2}}^{0.5}\right)^3} \quad (34)$$

$$k_{\mathrm{CH_4,m}} = 4.17 \times 10^6 \exp(-105000/\mathrm{RT}), \mathrm{kmol}/(\mathrm{kg}_{Ni}\ \mathrm{s}) \quad (35)$$

$$K_{\mathrm{CO,m}} = 5.8 \times 10^{-4} \exp(42000/\mathrm{RT}),\ \mathrm{bar}^{-0.5} \quad (36)$$

$$K_{\mathrm{H_2,m}} = 1.6 \times 10^{-2} \exp(16000/\mathrm{RT}),\ \mathrm{bar}^{-0.5} \quad (37)$$

For the oxygen carrier based on nickel oxide, carbon formation is strongly dependent on the availability of oxygen. When sufficient oxygen in the oxide is available there is limited formation of carbon independent of addition of steam or temperature in the range of 750–950°C. When more than 80% of the available oxygen is consumed, carbon began to form on the surface.[26] The kinetic model developed by Snoeck et al.,[27] based on a gradual dehydrogenation of molecularly adsorbed methane mechanism, was used to estimate the kinetics of methane cracking on a nickel catalyst. The rate-determining step was the abstraction of the first hydrogen atom from molecularly adsorbed methane with the formation of an adsorbed methyl group:

$$r_{\mathrm{cd}} = \frac{k_{\mathrm{cd}} K_{\mathrm{CH_4,cd}} \left(P_{\mathrm{CH_4}} - \frac{P_{\mathrm{H_2}}^2}{K_{\mathrm{p,cd}}}\right)}{\left(1 + \frac{1}{K''_{\mathrm{r,cd}}} P_{\mathrm{H_2}}^{3/2} + K_{\mathrm{CH_4,cd}} P_{\mathrm{CH_4}}\right)^2} \quad (38)$$

$$k_{\mathrm{cd}} = 43.4 \exp(-58900/\mathrm{RT}),\ \mathrm{kmolC}/\mathrm{kg_{Ni}\ s} \quad (39)$$

$$K_{\mathrm{p,cd}} = \exp(104/R) \times \exp(-88400/\mathrm{RT}) \quad (40)$$

$$K_{\mathrm{CH_4,cd}} = 2.1 \times 10^{-6} \exp(78000/\mathrm{RT}),\ \mathrm{bar}^{-1} \quad (41)$$

$$K'_{\mathrm{r,cd}} = 5.18 \times 10^7 \exp(-133000/\mathrm{RT}),\ \mathrm{bar}^{3/2} \quad (42)$$

The kinetic model developed by Snoeck et al.,[28] based on adsorption and dissociation of water and considering uniform carbon concentration in the nickel particle, was used to estimate the kinetics of carbon gasification with H_2O. The reaction of an adsorbed carbon atom with and adsorbed oxygen atom was chosen as the rate-determining step:

$$r_{\mathrm{g,H_2O}} = \frac{\frac{k_{\mathrm{g,H_2O}}}{K_{\mathrm{H_2O,g,H_2O}}} \left(\frac{P_{\mathrm{H_2O}}}{P_{\mathrm{H_2}}} - \frac{P_{\mathrm{CO}}}{K_{\mathrm{p,g,H_2O}}}\right)}{\left(1 + K_{\mathrm{CH_4,g,H_2O}} P_{\mathrm{CH_4}} + \frac{1}{K_{\mathrm{H_2O,g,H_2O}}} \frac{P_{\mathrm{H_2O}}}{P_{\mathrm{H_2}}} + \frac{1}{K''_{\mathrm{r,g,H_2O}}} P_{\mathrm{H_2}}^{3/2}\right)^2} \quad (43)$$

$$k_{\mathrm{g,H_2O}} = 3.08 \times 10^4 \exp(-166000/\mathrm{RT}),\ \mathrm{kmolC}/\mathrm{kg_{Ni}\ s} \quad (44)$$

$$K_{\mathrm{H_2O,g,H_2O}} = 4.73 \times 10^{-6} \exp(97700/\mathrm{RT}), \quad (45)$$

$$K_{\mathrm{CH_4,g,H_2O}} = 3.49\ \mathrm{bar}^{-1} \quad (46)$$

$$K''_{\mathrm{r,g,H_2O}} = 1.83 \times 10^{13} \exp(-216000/\mathrm{RT}) \quad (47)$$

$$K_{\mathrm{p,g,H_2O}} = \exp(137/R) \times \exp(-126000/\mathrm{RT}) \quad (48)$$

Carbon gasification with CO_2 kinetics was described by the model developed by Snoeck et al.[28] based on the

Table 3. Activation Energies and Pre-exponential Factors for the Final Model: Catalytic Gas–Solid Reactions

	E_{rf,H_2O} (kJ/mol)	E_{WGS} (kJ/mol)	$E_{g,HO}$ (kJ/mol)	E_{g,CO_2} (kJ/mol)	$k_{rf,H_2O,0} \times 10^{-6}$	$k_{WGS,0} \times 10^{2}$	$k_{g,H_2O,0} \times 10^{-4}$	$k_{g,CO_2,0} \times 10^{-10}$
Estimate	209.0	15.4	166.0	312.0	6.237	3.8	3.08	8.37
UL	215.9	20.6	167.4	316.7	14.24	5.97	3.65	14.5
LL	202.1	10.2	164.6	307.3	2.71	2.40	2.59	4.9

UL, upper limit; LL, lower limit of approximate 95% confidence interval.

following mechanism: molecular adsorption of CO, carbon formation from adsorbed CO, reaction of adsorbed oxygen with adsorbed CO as rate-determining step:

$$r_{g,CO_2} = \frac{\frac{k_{g,CO_2}}{K_{CO_2,g,CO_2}K_{CO,g,CO_2}}\left(\frac{P_{CO_2}}{P_{CO}} - \frac{P_{CO_2}}{K_{p,g,CO_2}}\right)}{\left(1 + K_{CO,g,CO_2}P_{CO} + \frac{1}{K_{CO_2,g,CO_2}K_{CO,g,CO_2}}\frac{P_{CO_2}}{P_{CO}}\right)^2} \quad (49)$$

$$k_{g,CO_2} = 8.37 \times 10^{10}\exp(-312000/\mathrm{RT}),\ \mathrm{kmolC/kg_{Ni}\ s} \quad (50)$$

$$K_{CO,g,CO_2} = 37.8 \times 10^{-6}\exp(100000/\mathrm{RT}),\ \mathrm{bar}^{-1} \quad (51)$$

$$K_{CO_2,g,CO_2} = 8.17 \times 10^{7}\exp(-104000/\mathrm{RT}),\ \mathrm{bar} \quad (52)$$

$$K_{p,g,CO_2} = \exp(178/R) \times \exp(-169000/\mathrm{RT}) \quad (53)$$

The rate parameters of the catalytic gas–solid kinetic models (k_{rf,H_2O}, k_{WGS}, k_{g,H_2o}, and k_{g,CO_2}) were obtained by means of nonlinear regression of the experimental data using Powell's algorithm. The parameters were tested by their 95% confidence interval and by physicochemical criteria such as the Arrhenius law.[29] Table 3 shows the reforming and gasification rate parameters and approximate 95% confidence intervals. The parity diagram is shown in Figure 6b.

Fixed bed microreactor mathematical model—transient kinetics

The method used for the calculation of the rate parameters of the noncatalytic and catalytic kinetics is based on the least-squares fit of the experimental output (components mole fraction) response with the microreactor model predicted response. Because more than one measurable quantity is available and their magnitude may differ considerably a weighted nonlinear least-squares was used. Powell's direct search technique was used to minimize the following relative square error function[30]:

$$F = \sqrt{\frac{\sum_i^m \sum_j^n \omega_{j,i}\left[\frac{y_j(t_i)\big|_{z=H} - y_{j,\exp}(t_i)\big|_{z=H}}{y_{j,\exp}(t_i)\big|_{z=H}}\right]^2}{mn}} \quad (54)$$

This function assigns an equal importance to the entire output signal from the reactor, which also takes into account the tail. The theoretical output response was calculated by solving the microreactor model equations.

The experimental outlet gas concentration signal is delayed because of the residence time of the gases between the valve and the gas analyzer. This residence time is (12 s in the case of our experiments. The residence time distribution experiments were conducted with oxygen as the tracer gas (step signal) and recording the oxygen breakthrough on the mass spectrometer.

Because the *Pe* number calculated from the dispersion coefficients in dispersion model is in order of 200, we considered that plug flow is a reasonable flow model to describe the microreactor comportment. Given that particle sizes used in CLC fixed bed microreactor are distributed around 140 μm, intraparticle temperature and concentration gradients can be neglected.

Under the foregoing assumptions, the unsteady-state species balance equations for the gas and solid phases and the corresponding boundary and initial conditions are formulated below:

$$\varepsilon_g\frac{\partial C_{CH_4}}{\partial t} + u_{SG}\frac{\partial C_{CH_4}}{\partial z} = \{-a_0(1-X)(k_{s1}+k_{s4})C_{CH_4}C_{NiO} - \left(r_{rf,H_2O} - r_{CH_4,m} + r_{rf,CO_2} + r_{cd}\right)\}C_{Ni}\rho_{oc} \quad (55)$$

$$\varepsilon_g\frac{\partial C_{H_2}}{\partial t} + u_{SG}\frac{\partial C_{H_2}}{\partial z} = \left\{\begin{array}{l} a_0(1-X)[(2k_{s1}+2k_{s4})C_{CH_4} - k_{s2}C_{H_2}/C_{Ni}]C_{NiO} + \\ +3r_{rf,H_2O}C_{Ni}\rho_{oc} + r_{WGS} - 3r_{CH_4,m} + 2r_{rf,CO_2} + 2r_{cd} + r_{g,H_2O} \end{array}\right\} \times C_{Ni}\rho_{oc} \quad (56)$$

$$\varepsilon_g\frac{\partial C_{H_2O}}{\partial t} + u_{SG}\frac{\partial C_{H_2O}}{\partial z} = \{a_0(1-X)k_{s2}C_{H_2}C_{NiO}/C_{Ni} - r_{rf,H_2O} - r_{WGS} + r_{CH_4,m} - r_{g,H_2O}\}C_{Ni}\rho_{oc} \quad (57)$$

$$\varepsilon_g\frac{\partial C_{CO}}{\partial t} + u_{SG}\frac{\partial C_{CO}}{\partial z} = \left\{\begin{array}{l} -a_0(1-X)[k_{s3}C_{CO}/C_{Ni} - k_{s4}C_{CH_4}]C_{NiO} \\ +r_{rf,H_2O} - r_{WGS} - r_{CH_4,m} + 2r_{rf,CO_2} + 2r_{g,CO_2} + r_{g,H_2O} \end{array}\right\} \times C_{Ni}\rho_{oc} \quad (58)$$

$$\varepsilon_g\frac{\partial C_{CO_2}}{\partial t} + u_{SG}\frac{\partial C_{CO_2}}{\partial z} = \{a_0(1-X)[k_{s1}C_{CH_4} + k_{s3}C_{CO}/C_{Ni}]C_{NiO} + r_{WGS} - r_{rf,CO_2} - r_{g,CO_2}\}C_{Ni}\rho_{oc} \quad (59)$$

$$\varepsilon_g\frac{\partial C_{Ar}}{\partial t} + u_{SG}\frac{\partial C_{Ar}}{\partial z} = 0 \quad (60)$$

$$\frac{\partial C_C}{\partial t} = r_{cd}C_{Ni}M_C - r_{g,CO2}C_{Ni}M_C - r_{g,H_2O}C_{Ni}M_C \quad (61)$$

$$t = 0 \quad C_{Ar} = C_{Ar}^0 \quad C_j = 0 \quad j = \mathrm{CH_4,\ H_2,\ CO,\ CO_2,\ H_2O} \quad (62)$$

$$C_{NiO} = C_{NiO}^0 \quad C_{Ni} = 0 \quad C_C = 0 \quad X = 0 \quad (63)$$

$$z = 0 \quad C_{CH_4} = C_{CH_4}^0 \quad C_{Ar} = C_{Ar}^0 \quad C_j = 0 \quad j = \mathrm{H_2,\ CO,\ CO_2,\ H_2O} \quad (64)$$

The partial differential equations were discretized in the axial direction using the second order central finite

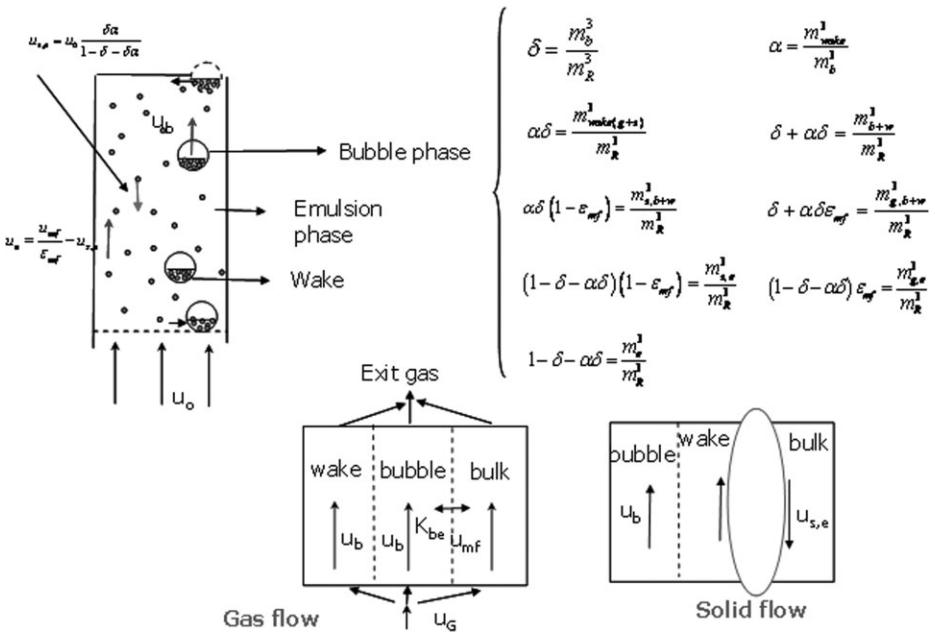

Figure 7. Fluidized bed reactor physical model.

difference method and the resulting set of coupled ordinary differential equations were integrated using GEAR method.

Fluidized bed reactor model

The model for the gas flow follows the description of three-phase model,[31] which considers that the gas rises in the emulsion at a relative velocity given by minimum fluidizing conditions, and the remaining gas rises in the bubbles (Figure 7). The gas volume increase, due to reaction, was taken into account and gas in the bubbles, according to the Davidson and Harrison[32] bubble model, was continuously recalculated through the height of the reactor. The bubble carries with its rising movement a certain amount of solid in the wake. The equations employed to estimate the minimum fluidization velocity, bubble size, bubble rising velocity, volumetric fraction of bubbles in the bed, the gas exchange coefficient between bubbles and emulsion, the solid exchange coefficient between wake and emulsion, and other parameters that appear in the fluid dynamic model are given in Table 4. A value of 0.15 has been considered for α (volumetric fraction of wake in bubbles).[33] Although some attempts to correlate α with d_b have been published,[34,35] the large dispersion in the experimental values makes it difficult to predict this parameter with precision. However, a variation of α between 0.05 and 0.15 results in small changes in reactor conversion.

From the flow models described above for the gas and the solid, and taking into account the reaction kinetics, the following mass balances in unsteady state can be obtained in a given control volume. The following differential equations contains three terms, corresponding to the mass transfer by convection, the exchange between phases, and the reaction, respectively:

Gas: bubble + wake

$$(\delta+\alpha\delta\varepsilon_{\mathrm{mf}})\frac{\partial C_{j,\mathrm{b}}}{\partial t}+\frac{\partial}{\partial z}\left[u_{\mathrm{b}}(\delta+\alpha\delta\varepsilon_{\mathrm{mf}})C_{j,\mathrm{b}}\right]=K_{j,\mathrm{be}}\left(C_{j,\mathrm{e}}-C_{j,\mathrm{b}}\right)(\delta+\alpha\delta\varepsilon_{\mathrm{mf}})+\left(\lambda_1 C_{j,\mathrm{b}}+\lambda_2 C_{j,\mathrm{e}}\right)\frac{\partial}{\partial z}\left[u_{\mathrm{b}}(\delta+\alpha\delta\varepsilon_{\mathrm{mf}})\right]+R_{j,\mathrm{b}}\left(C_{j,\mathrm{b}}\right)\rho_{\mathrm{p}}\alpha\delta(1-\varepsilon_{\mathrm{mf}}) \quad (65)$$

where $j = \mathrm{CH_4,H_2,H_2O,CO,CO_2,Ar}$

Gas: emulsion

$$(1-\delta-\alpha\delta)\varepsilon_{\mathrm{mf}}\frac{\partial C_{j,\mathrm{e}}}{\partial t}+\frac{\partial}{\partial z}\left[u_{\mathrm{e}}(1-\delta-\alpha\delta)\varepsilon_{\mathrm{mf}}C_{j,\mathrm{e}}\right]=K_{j,\mathrm{eb}}\left(C_{j,\mathrm{b}}-C_{j,\mathrm{e}}\right)(1-\delta-\alpha\delta)\varepsilon_{\mathrm{mf}}-\left(\lambda_1 C_{j,\mathrm{b}}+\lambda_2 C_{j,\mathrm{e}}\right)\frac{\partial}{\partial z}\left[u_{\mathrm{b}}(\delta+\alpha\delta\varepsilon_{\mathrm{mf}})\right]+R_{j,\mathrm{e}}\left(C_{j,\mathrm{e}}\right)\rho_{\mathrm{p}}(1-\delta-\alpha\delta)(1-\varepsilon_{\mathrm{mf}}) \quad (66)$$

Solid: wake

$$\alpha\delta(1-\varepsilon_{\mathrm{mf}})\rho_{\mathrm{p}}\frac{\partial C_{\mathrm{Ni,w}}}{\partial t}+\frac{\partial}{\partial z}\left[u_{\mathrm{b}}\alpha\delta(1-\varepsilon_{\mathrm{mf}})\rho_{\mathrm{p}}C_{\mathrm{Ni,w}}\right]=K_{j,\mathrm{we}}\left(C_{\mathrm{Ni,e}}-C_{\mathrm{Ni,w}}\right)\rho_{\mathrm{p}}\alpha\delta(1-\varepsilon_{\mathrm{mf}})+\left(\lambda_1 C_{\mathrm{Ni,w}}+\lambda_2 C_{\mathrm{Ni,e}}\right)\frac{\partial}{\partial z}\left[u_{\mathrm{b}}\alpha\delta(1-\varepsilon_{\mathrm{mf}})\rho_{\mathrm{p}}\right]+R_{\mathrm{Ni,w}}M_{\mathrm{Ni}}\rho_{\mathrm{p}}\alpha\delta(1-\varepsilon_{\mathrm{mf}}) \quad (67)$$

Table 4. Fluidized Bed Reactor Model—Fluid Dynamic Model

Minimum fluidization velocity[44] — Ergun equation

$$\frac{Ar}{Re} = 150\frac{1-\varepsilon_{mf}}{\phi^2\varepsilon_{mf}^3} + 1.75\frac{Re}{\phi\varepsilon_{mf}^3} \tag{T1}$$

where,

$$Ar = \frac{d_p^3\rho_g(\rho_p-\rho_g)g}{\mu_g^2} \qquad Re = \frac{\rho_g u_{mf} d_p}{\mu_g}$$

Rise velocity for bubbles[32]

$$u_b = u_{SG} - u_{mf} + 0.711(gd_b)^{1/2} \tag{T2}$$

Volumetric fraction of bubbles in the bed[31]

$$\delta = \frac{u_{SG}-u_{mf}}{u_b} \tag{T3}$$

Bed porosity[31]

$$\varepsilon = \delta\varepsilon_b + (1-\delta)\varepsilon_e = \delta + (1-\delta)\varepsilon_{mf} \tag{T4}$$

Bubble diameter[46]

$$d_b = \left[0.46\frac{(u_{SG}-u_{mf})^{0.5}z}{g^{0.25}} + d_{b0}^{1.25}\right]^{4/3} \tag{T5}$$

where:

$$d_{b0} = \frac{3.77(u_{SG}-u_{mf})^3}{g} \tag{T6}$$

for porous plate distributor[46]

Gas exchange between bubble and emulsion[31]

$$K_{bc,j} = 4.5\left(\frac{u_{mf}}{d_b}\right) + 5.85\left(\frac{D_j^{0.5}g^{0.25}}{d_b^{5/4}}\right) \qquad K_{ce,j} = 6.78\left(\varepsilon_{mf}D_j u_b\right)^{1/2} \tag{T7}$$

$$\frac{1}{K_{be,j}} \approx \frac{1}{K_{bc,j}} + \frac{1}{K_{ce,j}} \tag{T8}$$

Solid exchange between wake and emulsion[47]

$$K_{we,j} = \frac{0.075(u_{SG}-u_{mf})}{u_{mf}d_b} \quad \text{if} \quad u_{SG}/u_{mf} \le 3 \tag{T9}$$

$$K_{we,j} = \frac{0.15}{d_b} \quad \text{if} \quad u_{SG}/u_{mf} > 3 \tag{T10}$$

$$\alpha\delta(1-\varepsilon_{mf})\rho_p\frac{\partial C_{NiO,w}}{\partial t} + \frac{\partial}{\partial z}\left[u_b\alpha\delta(1-\varepsilon_{mf})\rho_p C_{NiO,w}\right] = K_{j,we}\left(C_{NiO,e}-C_{NiO,w}\right)\rho_p\alpha\delta(1-\varepsilon_{mf}) + \left(\lambda_1 C_{NiO,w}+\lambda_2 C_{NiO,e}\right)\frac{\partial}{\partial z}\left(u_b\alpha\delta(1-\varepsilon_{mf})\rho_p\right) - R_{NiO,w}M_{NiO}\rho_p\alpha\delta(1-\varepsilon_{mf}) \tag{68}$$

$$\alpha\delta(1-\varepsilon_{mf})\rho_p\frac{\partial C_{C,w}}{\partial t} + \frac{\partial}{\partial z}\left[u_b\alpha\delta(1-\varepsilon_{mf})\rho_p C_{C,w}\right] = K_{j,we}\left(C_{C,e}-C_{C,w}\right)\rho_p\alpha\delta(1-\varepsilon_{mf}) + \left(\lambda_1 C_{C,w}+\lambda_2 C_{C,e}\right)\frac{\partial}{\partial z}\left(u_b\alpha\delta(1-\varepsilon_{mf})\rho_p\right) + R_{C,w}M_C\rho_p\alpha\delta(1-\varepsilon_{mf}) \tag{69}$$

Solid: emulsion

$$(1-\delta-\alpha\delta)(1-\varepsilon_{mf})\rho_p\frac{\partial C_{Ni,e}}{\partial t} + \frac{\partial}{\partial z}\left[u_{s,e}(1-\delta-\alpha\delta)(1-\varepsilon_{mf})\rho_p C_{Ni,e}\right] = K_{j,ew}\left(C_{Ni,w}-C_{Ni,e}\right)\rho_p(1-\delta-\alpha\delta)(1-\varepsilon_{mf}) - \left(\lambda_1 C_{Ni,w}+\lambda_2 C_{Ni,e}\right)\frac{\partial}{\partial z}\left[u_b\alpha\delta(1-\varepsilon_{mf})\rho_p\right] + R_{Ni,e}M_{Ni}\rho_p(1-\delta-\alpha\delta)(1-\varepsilon_{mf}) \tag{70}$$

$$(1-\delta-\alpha\delta)(1-\varepsilon_{mf})\rho_p\frac{\partial C_{NiO,e}}{\partial t} + \frac{\partial}{\partial z}\left[u_{s,e}(1-\delta-\alpha\delta)(1-\varepsilon_{mf})\rho_p C_{NiO,e}\right] = K_{j,ew}\left(C_{NiO,w}-C_{NiO,e}\right)\rho_p(1-\delta-\alpha\delta)(1-\varepsilon_{mf}) - \left(\lambda_1 C_{NiO,w}+\lambda_2 C_{NiO,e}\right)\frac{\partial}{\partial z}\left[u_b\alpha\delta(1-\varepsilon_{mf})\rho_p\right] - R_{NiO,e}M_{NiO}\rho_p(1-\delta-\alpha\delta)(1-\varepsilon_{mf}) \tag{71}$$

$$(1-\delta-\alpha\delta)(1-\varepsilon_{mf})\rho_p\frac{\partial C_{C,e}}{\partial t} + \frac{\partial}{\partial z}\left[u_{s,e}(1-\delta-\alpha\delta)(1-\varepsilon_{mf})\rho_p C_{C,e}\right] = K_{j,ew}\left(C_{C,w}-C_{C,e}\right)\rho_p(1-\delta-\alpha\delta)(1-\varepsilon_{mf}) - \left(\lambda_1 C_{C,w}+\lambda_2 C_{C,e}\right)\frac{\partial}{\partial z}\left[u_b\alpha\delta(1-\varepsilon_{mf})\rho_p\right] + R_{C,e}M_C\rho_p(1-\delta-\alpha\delta)(1-\varepsilon_{mf}). \tag{72}$$

The reaction terms are the followings:

$$R_{CH_4,i} = \{-a_0(1-X)(k_{s1}+k_{s4}) - r_{rf,H_2O,i} + r_{CH_4,m,i} - r_{rf,CO_2,i} - r_{cd,i}\}C_{Ni,k} \tag{73}$$

$$R_{H_2,i} = \left\{\begin{matrix} a_0(1-X)\left[2(k_{s1}+k_{s4})C_{CH_4,i} - k_{s2}C_{H_2,i}/C_{Ni,k}\right]C_{NiO,k} \\ +3r_{rf,H_2O,i} + r_{WGS,i} - 3r_{CH_4,m,i} + 2r_{rf,CO_2,i} + 2r_{cd,i} + r_{g,H_2O,i} \end{matrix}\right\} \times C_{Ni,k} \tag{74}$$

$$R_{H_2O,i} = \{a_0(1-X)k_{s2}C_{H_2,i}C_{NiO,k}/C_{Ni,k} - r_{rf,H_2O,i} - r_{WGS,i} - r_{g,H_2O,i}\}\ C_{Ni,k} \tag{75}$$

$$R_{CO,i} = \left\{\begin{matrix} -a_0(1-X)\left[k_{s3}C_{CO,i}/C_{Ni,k} - k_{s4}C_{CH_4,i}\right]C_{NiO,k} \\ +r_{rf,H_2O,i} - r_{WGS,i} - r_{CH_4,m,i} + 2r_{rf,CO_2,i} + 2r_{g,CO_2,i} + r_{g,H_2O,i} \end{matrix}\right\} \times C_{Ni,k} \tag{76}$$

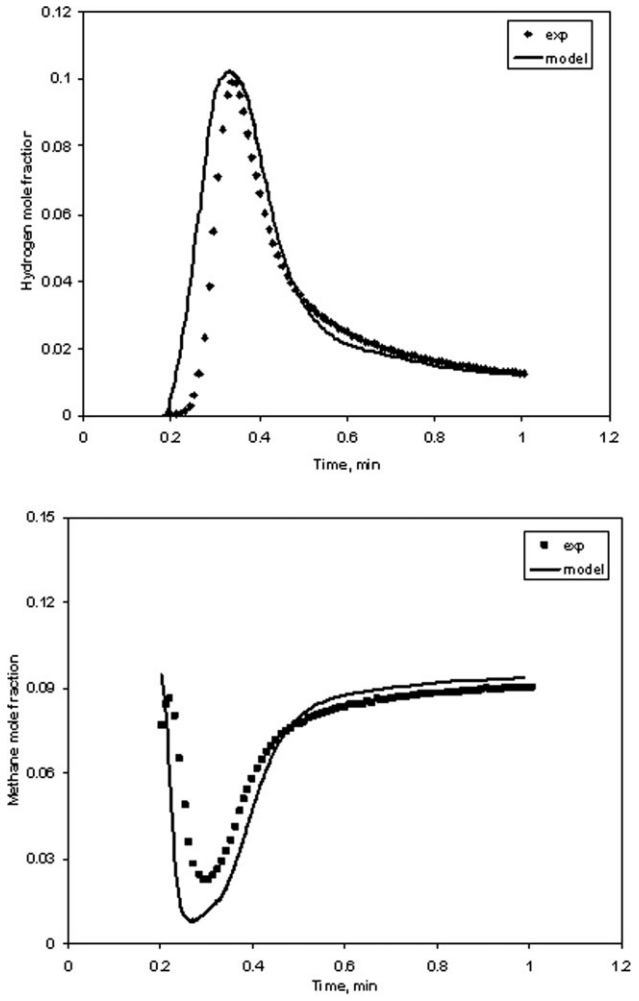

Figure 8. Experimental vs. calculated hydrogen and methane mole fraction obtained during the reduction with CH_4 (10%) of Ni15-Al_2O_3 in fixed bed microreactor at 700°C (wet basis, u_{SG} = 0.473 m/s, NiO conversion = 0.94).

$$R_{CO_2,i} = \{a_0(1-X)\left[k_{s1}C_{CH_4,i} + k_{s3}C_{CO,i}/C_{Ni,k}\right]C_{NiO,k} + r_{WGS,i} - r_{rf,CO_2,i} - r_{g,CO_2,i}\}C_{Ni,k} \quad (77)$$

where k = w if i = b; k = e if i = e

$$R_{NiO,i} = a_0(1-X)[(2k_{s1}+k_{s4})C_{CH_4}C_{Ni} + k_{s2}C_{H_2} + k_{s3}C_{CO}]C_{NiO} \quad (78)$$

$$R_{Ni,i} = a_0(1-X)[(2k_{s1}+k_{s4})C_{CH_4}C_{Ni} + k_{s2}C_{H_2} + k_{s3}C_{CO}]C_{NiO} \quad (79)$$

$$R_{C,i} = \left(r_{cd} - r_{g,CO_2} - r_{g,H_2O}\right)C_{Ni} \quad (80)$$

where $i = w, e$.

The terms $(\lambda_1 C_{j,b} + \lambda_2 C_{j,e})\frac{\partial}{\partial z}[u_b(\delta + \alpha\delta\varepsilon_{mf})]$ and $(\lambda_1 C_{j,w} + \lambda_2 C_{j,e})\frac{\partial}{\partial z}\left[u_b\alpha\delta(1-\varepsilon_{mf})\rho_p\right]$ take into account the gas and solid crossflow between bubble/wake and emulsion as a consequence of the variation of bubbles properties with height.[33,36] A change in the volume in the bubbles must be compensated by a net gas (or solid) flow from the emulsion to bubble and wake or vice versa. This is done as follows:

$$\lambda_1 = 1 \quad \lambda_2 = 0 \quad \text{when} \quad \frac{\partial(u_b\delta)}{\partial z} < 0 \quad (81)$$

$$\lambda_1 = 0 \quad \lambda_2 = 1 \quad \text{when} \quad \frac{\partial(u_b\delta)}{\partial z} \geq 0 \quad (82)$$

The initial and boundary conditions are

$$t = 0 \quad C_{Ar,i} = C^0_{Ar,i} \quad C_{j,i} = 0 \quad j = CH_4, H_2, CO, CO_2, H_2O \quad (83)$$

$$C_{NiO,i} = C^0_{NiO,i} \quad C_{Ni,i} = 0 \quad C_{C,i} = 0 \quad (84)$$

$$z = 0 \quad C_{CH_4,i} = C^0_{CH_4,i} \quad C_{Ar,i} = C^0_{Ar,i} \quad C_{j,i} = 0 \quad j = H_2, CO, CO_2, H_2O \quad (85)$$

$$C_{j,w} = C_{j,e} \quad \frac{\partial C_{j,e}}{\partial z} = 0 \quad \text{where } j = Ni, NiO, C \quad (86)$$

$$z = H \quad C_{j,e} = C_{j,w} \quad \frac{\partial C_{j,w}}{\partial z} = 0 \quad \text{where } j = Ni, NiO, C \quad (87)$$

The partial differential equations were discretized in the axial direction using the second order central finite difference method and the resulting set of coupled ordinary differential equations were integrated using GEAR method.

Results and Discussion

Fixed bed microreactor—transient reduction kinetics

Noncatalytic gas–solid reactions could be controlled by external mass transfer, gas diffusion into the porous particles, and chemical reaction. External mass transfer resistance was reduced as much as possible by working with high gas flow rates and a small quantity of oxygen carrier in the kinetic experiments. The average particle size was around 140 μm and this suggests that internal diffusion resistance was negligible compared to the reaction rate.[37] Thus, the noncatalytic gas–solid reactions kinetics was fitted assuming kinetic control. The values of the activation energy for the reduction reactions varied between 23.6 and 77.4 kJ/mol: 23.6 kJ/mol—partial oxidation of CH_4 to CO, 26.1 kJ / mol—reduction of NiO with H_2, 26.5 kJ/mol—reduction of NiO with CO, and 77.4 kJ/mol—reduction of NiO with CH_4 to CO_2 and H_2. These values are in good agreement with the literature: reduction of NiO with H_2: 26 kJ/mol (Mattisson et al.[38]), 26 kJ/mol (Abad et al.[39]); reduction of NiO with CO: 25 kJ/mol (Mattisson et al.[38]), 25 kJ/mol (Abad et al.[39]); reduction of NiO with CH_4: 78 kJ/mol (Abad et al.[39]), 82 kJ/mol (Ishida et al.[40]).

The kinetics of the catalytic gas–solid reactions was evaluated using representative LHHW models of the literature. Several reaction rate constants were re-evaluated under CLC conditions using the experimental data obtained in fixed bed microreactor. The activation energies are forced to be similar with the values of the original models.

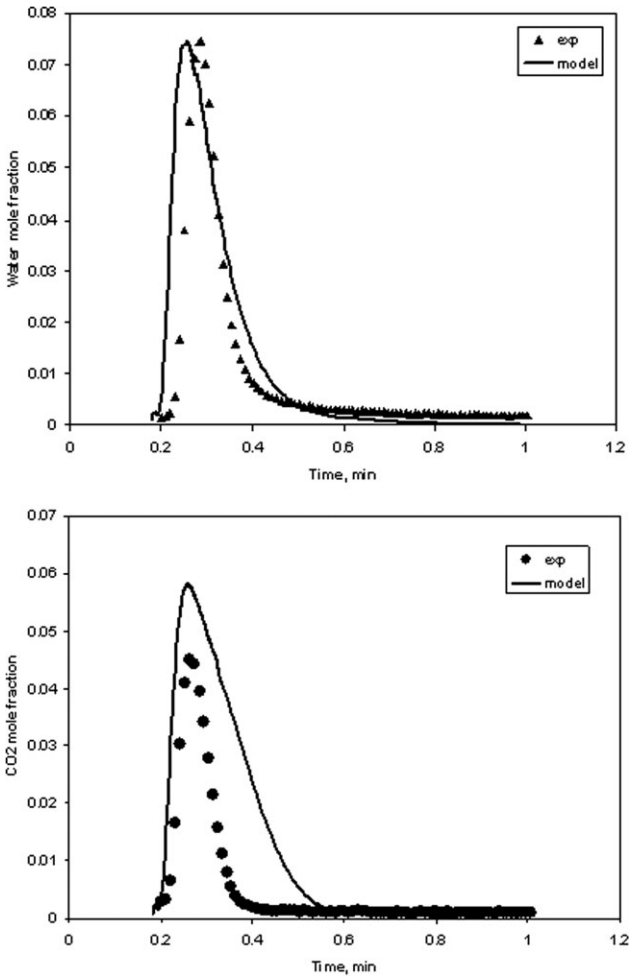

Figure 9. Experimental vs. calculated water and carbon dioxide mole fraction obtained during the reduction with CH_4 (10%) of Ni15-Al_2O_3 in fixed bed microreactor at 700°C (wet basis, u_{SG} = 0.473 m/s, NiO conversion = 0.94).

Figures 5, 8–11 show gas product distribution obtained during the reduction step of NiO–Al_2O_3 oxygen carrier at temperatures from 600 to 900°C. The comparison between experimental and calculated results shows a similar gas product distribution (Figures 8–11). The difference between water prediction and experimental result can be explained by the difficulty to calibrate water on the mass spectrometer and the condensation of H_2O prior to the mass spectrometer. Oxygen carrier conversion varies between 0.88 and 0.96. The length of the reduction period is 60 s. The outlet gas concentration signal is delayed by 10–12 s depending on the flow rate of the gas because of the residence time of the gas between the three-way valve and the gas analyser (the simulated mole fraction was corrected taking into account the time delay). During the first 6 s of the reduction period (except at T = 600°C when the CH_4 methane activation is longer) almost all of the reacted CH_4 is converted to CO_2, CO, H_2, and H_2O. The presence of H_2 simultaneously with water suggests that the complete methane combustion to H_2O takes place through H_2 formation in a two-step process (reactions 1 and 2). Also, the presence of CO simultaneously with CO_2 suggests that the complete methane oxidation to CO_2 takes place indirectly with CO as an intermediate state in a two-step process (reactions 3 and 4). On the other side, CH_4 react directly to CO_2, without CO as intermediate state (reaction 1). Figures 5, 10, and 11 show a similar amount of CO for a large temperature field. A possible explanation of this behavior could be the fact that the effect of the temperature on the reactions 3 and 4 is similar (the activation energies are comparable 26.5 and 23.6 kJ/mol, respectively). Also, at the beginning of the reduction period, CO and H_2 could be generated by the catalytic reactions. As the reactions proceeds, the oxygen in the particles is depleted, and the outlet concentrations of CO_2, H_2, and H_2O decrease, whereas the concentration of CH_4 increases. The subsequent slow decrease of the CO concentration and the peaks of CO and CO_2 in the oxidation period (Figure 12) indicate carbon formation during the previous reduction period. At higher temperature, the gas distribution show similar features, the only apparent differences are the decrease of the length of the activation process during the initial stages of methane contact with the carrier and the move of the minimum in the

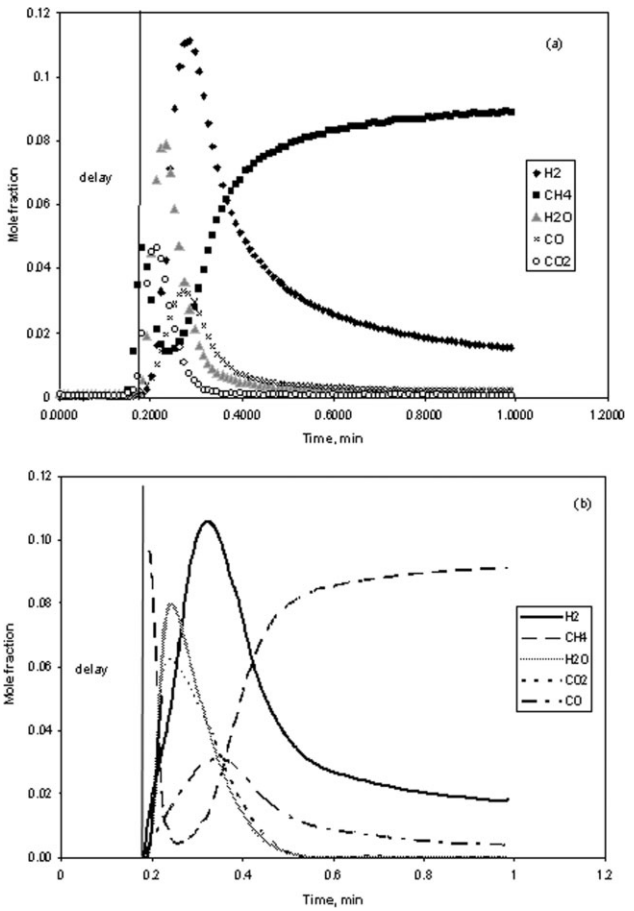

Figure 10. Experimental (a) and calculated (b) gas product distribution obtained during the reduction with CH_4 (10%) of Ni15-Al_2O_3 in fixed bed microreactor at 800°C (wet basis, u_{SG} = 0.521 m/s, NiO conversion = 0.95).

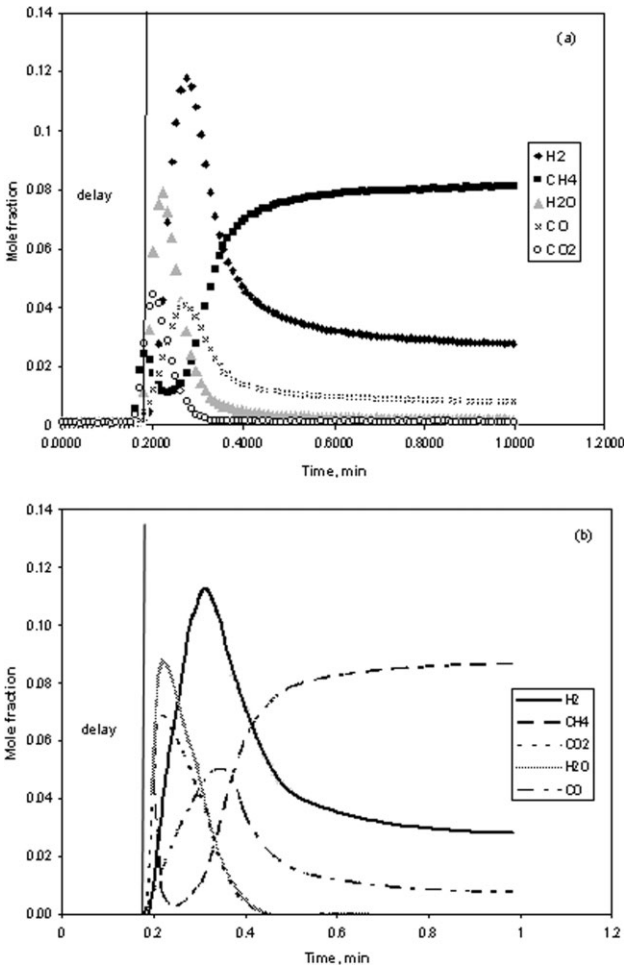

Figure 11. Experimental (a) and calculated (b) gas product distribution obtained during the reduction with CH_4 (10%) of Ni15-Al_2O_3 in fixed bed microreactor at 900°C (wet basis, u_{SG} = 0.57 m/s, NiO conversion = 0.96).

CH_4 curves to lower values, indicating higher carrier reactivity for the reduction step.

In CLC, the carbon deposition on the solid carrier may limit the efficiency of the total CO_2 capture.[41] Therefore, it is important not only to understand the possible carbon mechanisms but also to investigate the operating strategies that need to be implemented to minimize/avoid carbon formation. Side reactions might occur in CLC that result in the formation of solid carbon on the oxygen carrier particles (Figure 13). The conditions for which carbon formation is thermodynamically possible depend on the amount of oxygen added with the nickel oxide, fuel conversion as well the temperature and pressure.[26] There are two possible ways of carbon formation: methane decomposition or the Boudouard reaction. Kinetically, both pyrolysis and Boudouard reactions are known to have a limited importance in the absence of a catalyst, but both reactions can be readily catalyzed by nickel. Pyrolysis is an endothermic reaction, thermodynamically favored at high temperature and the exothermic Boudouard reaction is more likely to take at lower temperature. This was confirmed by Claridge et al.[42] and Jin et al.[43] which found that at higher temperature (600°C), the amount of carbon obtained from carbon monoxide via the Boudouard reaction is very slow compared to the amount deposited from methane decomposition. In our CLC experiments, the temperature is higher that 600 C, so only methane decomposition was considered responsible for the carbon deposition.

The carbon formation during the reduction period was calculated by integrating the total amounts of carbon dioxide and carbon monoxide produced during the oxidation period (because no source of oxygen was present in the inert period following the reduction period, the carbon formed in the reduction period was oxidized only in the oxidation period):

$$D_{M,\mathrm{CO_2,exp}} = u_{\mathrm{SG}} S \overline{C_{\mathrm{CO_2}}} \quad \text{where} \quad \overline{C_{\mathrm{CO_2}}} = \frac{\int_{t_0}^{t_{\mathrm{oxd}}} y_{\mathrm{CO_2}}\big|_{z=H}(t)\,\frac{P}{RT}\,\mathrm{d}t}{t_{\mathrm{oxd}} - t_0} \tag{88}$$

$$D_{M,\mathrm{CO,exp}} = u_{\mathrm{SG}} S \overline{C_{\mathrm{CO}}} \quad \text{where} \quad \overline{C_{\mathrm{CO}}} = \frac{\int_{t_0}^{t_{\mathrm{oxd}}} y_{\mathrm{CO}}\big|_{z=H}(t)\,\frac{P}{\mathrm{RT}}\,\mathrm{d}t}{t_{\mathrm{oxd}} - t_0} \tag{89}$$

$$\text{C production (kmol/s), exp} = D_{M,\mathrm{CO_2,exp}} + D_{M,\mathrm{CO,exp}} \tag{90}$$

where t_0 is the time when the oxidation period started and t_{oxd} is the time of oxidation period.

The theoretical carbon production during the reducing period was evaluated by the following equation:

$$\text{C production (kmol/s), model} = \frac{\overline{C_C}}{M_C}\rho_{\mathrm{oc}} V_{\mathrm{bed}} \frac{1}{t_{\mathrm{red}}} \quad \text{where } \overline{C_C} = \frac{\int_0^H C_C\,\mathrm{d}z}{H} \tag{91}$$

where t_{red} is the time of reduction period.

As expected, carbon deposition starts already at the beginning of the reduction stage of the CLC process, at first,

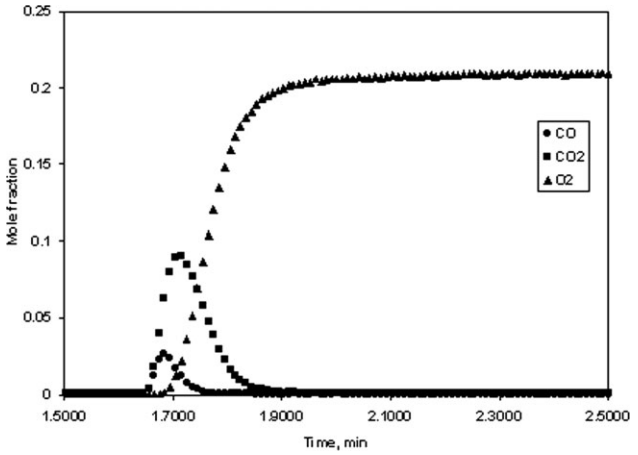

Figure 12. Experimental CO, CO_2, and O_2 gas product distribution during the oxidation period in fixed bed microreactor at 800°C.

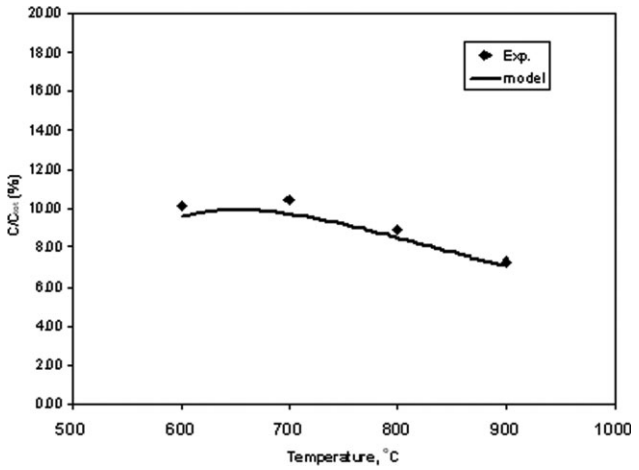

Figure 13. Experimental vs. calculated carbon formation ratio obtained during the reduction with CH_4 (10%) of Ni15-Al_2O_3 in fixed bed microreactor.

increasing with time almost linearly. However, at the beginning of the reduction period, carbon deposition is not significant due to the presence of the water which causes the steam reforming (reaction 5) and gas shift reactions (reaction 9). After water depletion period and after 80% of the available oxygen was consumed (almost all the microreactor bed is found in a reduced state), the carbon deposition rate increases dramatically and the solid carbon deposit dependents of the length of the reduction period. Carbon formation decreases with the increase of the temperature (Figure 13).

In fixed bed microreactor, the thermal decomposition of methane operates in clear competition with methane consumption with the main reactions of CLC. Metallic nickel catalyzes actively the carbon deposition on the carrier in the reactor bed, imposing some constrains to the use of this type of oxygen carrier and the need to optimize the operating conditions used.

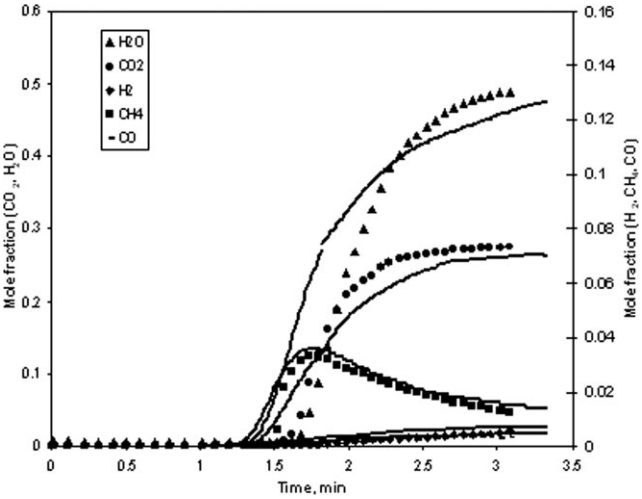

Figure 14. Experimental and calculated gas product distribution obtained during the reduction with CH_4 (50%) of Ni15-Al_2O_3 in fluidized bed at 623°C (wet basis, $u_{SG,in}$ = 0.033 m/s, H = 0.23 m, $u_{SG,in}/u_{mf}$ = 5, NiO conversion = 0.36).

The continuous lines are results predicted by the model using kinetic parameters obtained in this work.

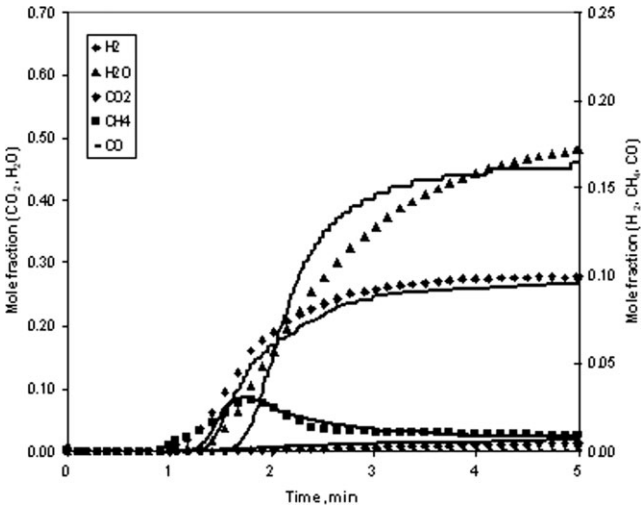

Figure 15. Experimental and calculated gas product distribution obtained during the reduction with CH_4 (50%) of Ni15-Al_2O_3 in fluidized bed at 645°C (wet basis, $u_{SG,in}$ = 0.034 m/s, H = 0.23 m, $u_{SG,in}/u_{mf}$ = 5.4, NiO conversion = 0.62).

The continuous lines are results predicted by the model using kinetic parameters obtained in this work.

Fluidized bed reactor—kinetic model validation

Reduction with Ni-based oxygen carrier was carried out in a batch-fluidized bed under experimental conditions similar to those used in fixed bed microreactor with the intention of the validation of the kinetic model developed in fixed bed microreactor.

The evolutions of the molar fractions of the different compounds detected experimentally in the outlet gas and predicted by the model during the reduction stage of a CLC cycle are shown in Figures 14–16. A comparison between the experimental and calculated results shows a similar gas product distribution and a good agreement (with the exception of water). The difference between water prediction and experimental result on Figures 14–16 can be explained by the difficulty to calibrate water on the mass spectrometer and the condensation of H_2O prior to the mass spectrometer. Contrary to the measurements, the results from the model respect the stoechiometry of the methane combustion.

It was found that H_2 emission from the fuel fluidized bed reactor was very small and that no CO emission was detected. The CH_4 conversion is complete over an excess of NiO and the outlet gas is formed largely by CO_2 and H_2O. Oxygen carrier conversion varies between 0.15 and 0.62 and is a function of the gas flow rate, CH_4 concentration and reduction time. It seems that all the experimental conditions correspond to the desired conditions as a result of low CO and H_2 emissions detected in the flue gas from the reduction reactor.

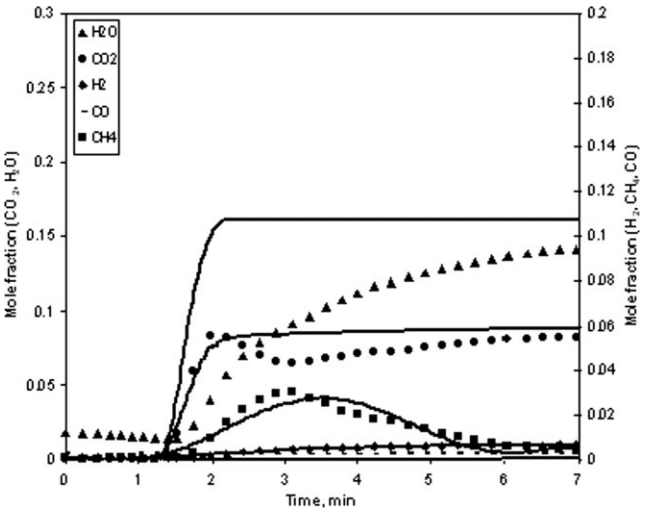

Figure 16. Experimental and calculated gas product distribution obtained during the reduction with CH_4 (10%) of Ni15-Al_2O_3 in fluidized bed at 810°C (wet basis, $u_{SG,in}$ = 0.04 m/s, H = 0.23 m, $u_{SG,in}/u_{mf}$ = 6, NiO conversion = 0.15).

The continuous lines are results predicted by the model using kinetic parameters obtained in this work.

Carbon deposition is not significant in the fluidized bed reactor because almost all the reactor bed is found in the conditions when the actual amount of oxygen added with the nickel oxide is higher that the stoechiometric amount needed for full conversion of CH_4 to CO_2 and H_2O. Furthermore the availability of metallic nickel which catalyzes the carbon deposition process is not significant and as a result carbon deposition rate has a limited importance.

Conclusions

The kinetics of reduction of NiO–Al_2O_3 oxygen carrier particles with CH_4 in a fixed bed microreactor has been investigated. A volumetric particle model with chemical reaction control was used to evaluate the noncatalytic gas–solid kinetics. The kinetics of the catalytic gas–solid reactions was evaluated using representative models of the literature and several reaction rate constants were re-evaluated under CLC conditions. The energy activation values for the noncatalytic gas–solid reduction reactions varied between 23.6 and 77.4 kJ/mol: 23.6 kJ/mol—partial oxidation of CH_4 to CO, 26.1 kJ /mol—reduction of NiO with H_2, 26.5 kJ/mol—reduction of NiO with CO, and 77.4 kJ/mol—reduction of NiO with CH_4 to CO_2 and H_2. The reduction of Ni-based oxygen carrier with CH_4 was also carried out in a fluidized bed reactor in experimental conditions similar to those exploited in fixed bed microreactor to validate the kinetic model proposed. A three-phase model was developed combining a relatively detailed hydrodynamics with the non catalytic and catalytic gas–solid reactions to simulate the comportment of CLC fluidized bed reactor.

The study of CLC of methane in fixed bed microreactor and fluidized bed reactor shows that the carrier reactivity is high at low temperatures typical to industrial processes such as refineries with almost complete conversion of the gas in fluidized bed. The complete methane combustion to H_2O and CO_2 takes place through H_2 and CO formation in a two-step process. Also, the methane reacts with NiO to produce H_2 and CO_2 directly, without CO as intermediate state. The reaction rate was a function of the reacting gas concentration, temperature, and the Ni content in oxygen carrier.

Carbon deposition occurred predominantly when oxygen carrier particles are in a high reduction state. In the fixed bed microreactor, the thermal decomposition of methane operates in clear competition with methane consumption with the main reactions of CLC. Metallic nickel catalyzes actively carbon deposition on the carrier in the reactor bed, imposing some constrains to the use of this type of oxygen carrier and the need to optimize the operating conditions used. Carbon deposition is not expected in fluidized bed reactor as long as sufficient metal oxide is supplied to the reduction reactor.

Notation

a_0 = initial specific surface area of the oxygen carrier, $m^2/kg_{carrier}$
C_j = bulk concentration of gaseous reactant, $kmol/m^3$
C_C = carbon concentration, kg $C/kg_{carrier}$
C_{Ni} = Ni concentration, kg $Ni/kg_{carrier}$
C_{NiO} = NiO concentration, kg $NiO/kg_{carrier}$
C'_{NiO} = NiO concentration, kmol $NiO/kg_{carrier}$
d_b = bubble diameter, m
d_{b0} = initial bubble diameter, m
d_p = particle diameter, m
D_j = diffusion coefficient of component j, m^2/s
$D_{M,j}$ = molar flow rate of component j, kmol/s
F = relative square error function
g = acceleration of gravity, m/s^2
H = fixed bed or fluidized bed height, m
k_{cd} = reaction rate constant for carbon deposition, $kmol/(kg_{Ni}\ s)$
$k_{CH_4,m}$ = reaction rate constant of CO methanation, $kmol/(kg_{Ni}\ s)$
k_{g,CO_2} = reaction rate constant for carbon gasification with CO_2, $kmol/(kg_{Ni}\ s)$
k_{g,H_2O} = reaction rate constant for carbon gasification with water, $kmol/(kg_{Ni}\ s)$
k_{rf,CO_2} = reaction rate constant of methane reforming with CO_2, $kmol/(kg_{Ni}\ s\ bar^2)$
k_{rf,H_2O} = reaction rate constant of methane reforming with H_2O, $kmol/(kg_{Ni}\ s\ bar^{0.25})$
k_{si} = chemical reaction rate constant, m/s
k_{WGS} = reaction rate constant of water gas shift reaction, $kmol/(kg_{Ni}\ s\ bar)$
$K_{j,bc}$ = gas exchange coefficient between bubble-cloud, s^{-1}
$K_{j,be}$ = gas exchange coefficient between bubble-emulsion, s^{-1}
$K_{j,ce}$ = gas exchange coefficient between cloud-emulsion, s^{-1}
$K_{CH_4,cd}$ = adsorption coefficient of CH_4 (carbon deposition), bar^{-1}
K_{CH_4,g,H_2O} = adsorption coefficient of CH_4 (carbon gasification with H_2O), bar^{-1}
K_{CO,g,CO_2} = adsorption coefficient of CO (carbon gasification with CO_2), bar^{-1}
K_{CO_2,g,CO_2} = adsorption coefficient of CO_2 (carbon gasification with CO_2), bar
$K_{CO,m}$ = adsorption coefficient of CO (methanation), $bar^{-0.5}$
K_{CO,rf,H_2O} = adsorption coefficient of CO (methane reforming with water), bar^{-1}
K_{CO_2,rf,CO_2} = adsorption coefficient of CO_2 (methane reforming with CO_2), bar^{-1}

$K_{j,eb}$ = gas exchange coefficient between emulsion-bubble, $K_{j,eb} = K_{j,be}(\delta + \delta\alpha\varepsilon_{mf})/(1 - \delta - \delta\alpha)\varepsilon_{mf}$, s^{-1}
$K_{j,ew}$ = coefficient of solid exchange between emulsion and wake per unit of solid volume in emulsion, $K_{j,ew} = K_{j,we}\delta\alpha/(1 - \delta - \delta\alpha)$, s^{-1}
K_{H_2O,g,H_2O} = adsorption coefficient of H_2O (carbon gasification with water), -
$K_{H_2,m}$ = adsorption coefficient of H_2 (methanation), $bar^{-0.5}$
K_{H_2,rf,H_2O} = adsorption coefficient of H_2 (methane reforming with water), $bar^{-0.5}$
K_{H_2O,rf,H_2O} = adsorption coefficient of H_2O (methane reforming with water), -
K_p = equilibrium constants
$K_{we,j}$ = coefficient of solid exchange between wake and emulsion, per unit of solid volume in wake, s^{-1}
m = number of mole fractions values compared
M_j = molecular mass of component j, kg/kmol
n = number of components
p_j = partial pressure, bar
r_{cd} = reaction rate for carbon deposition, $kmolC/kg_{Ni}$ s
$r_{CH_4,m}$ = reaction rate for methanation, $kmol/kg_{Ni}$ s
r_{g,CO_2} = reaction rate for carbon gasification with H_2O, $kmol/kg_{Ni}$ s
r_{g,H_2O} = reaction rate for carbon gasification with H_2O, $kmol/kg_{Ni}$ s
r_{rf,CO_2} = reaction rate for methane reforming with CO_2, $kmol/kg_{Ni}$ s
r_{rf,H_2O} = reaction rate for methane reforming with H_2O, $kmol/kg_{Ni}$ s
r_{mi} = reaction rate per unit mass of the oxygen carrier, $kmol/kg_{carrier}$s
r_{si} = specific surface reaction rate, $kmol/m^2_{carrier}$s
r_{WGS} = reaction rate for water gas shift reaction, $kmol/kg_{Ni}$ s
R = ideal gas constant, J/mol K
R_j = reaction rate of the component j per unit mass of the oxygen carrier, $kmol/kg_{carrier}$ s
S = reactor section, m^2
t = time, s
T = reaction temperature, K
u_b = bubble velocity, m/s
u_e = emulsion velocity, $u_e = u_{mf}/\varepsilon_{mf} - u_{s,e}$, m/s
$u_{s,e}$ = downward solid velocity in emulsion, $u_{s,e} = u_b\alpha\delta/[1 - \delta - \delta\alpha]$, m/s
u_{mf} = minimum fluidization velocity, m/s
u_{SG} = superficial gas velocity, m/s
V_{bed} = bed volume, m^3
X = NiO conversion
y_j = mole fraction of component j, $y_j = C_j/\sum_j C_j$
z = axial reactor coordinate, m

Greek letters

α = fraction of wake in bubbles
δ = fraction of bed in bubbles
ε = bed porosity
ε_b = bubble void fraction
ε_g = gas holdup
ε_e = void fraction of emulsion phase
ε_{mf} = minimum fluidization porosity
μ_a = α phase dynamic viscosity, kg/m.s
$\nu_{NiO,i}$ = stoichiometric coefficient of NiO in reaction i
ρ_g = gas density, kg/m^3
ρ_{oc} = fixed bed density, $kg_{carrier}/m^3_R$
ρ_p = particle density, $kg_{carrier}/m^3_p$
$\omega_{i,j}$ = weight factor

Subscripts

b = bubbles
g = gas phase
e = emulsion
in = inlet
p = solid particle
oc = oxygen carrier
w = wake

Literature Cited

1. Hossain MM, de Lasa HI. Chemical-looping combustion (CLC) for inherent CO2 separation—a review. *Chem Eng Sci* In press.
2. Ritcher H, Knoche R. *Reversibility of combustion process*. In: Gaggioli RA, editor. *Efficiency and Costing; Second Law Analysis of Process*, vol 235. ACS Symposium Series. Washington DC: American Chemical Society, 1983:71–86.
3. Garcia-Labiano F, Adanez J, de Diego LF, Gayan P, Abad A. Effect of pressure on the behavior of copper-, iron-, and nickel-based carriers for chemical-looping combustion. *Energy Fuels*. 2006;20:26–33.
4. Wolf J, Anheden M, Yan J. Comparison of nickel- and iron-based oxygen carriers in chemical looping combustion for CO_2 capture in power generation. *Fuel*. 2005;84:993–1006.
5. Mattisson T, Jardnas A, Lyngfelt A. Reactivity of some oxides supported on alumina with alternating methane and oxygen—application for chemical-looping combustion. *Energy Fuels*. 2003;17:643–651.
6. Mattisson T, Johansson M, Lyngfelt A. Multicycle reduction and oxidation of different types of iron oxide particles—Application to chemical-looping combustion. *Energy Fuels*. 2004;18:628–637.
7. Copeland R, Alptekin G, Cesario M, Gershanovich Y. *Sorbent energy transfer system (SETS) for CO_2 separation with high efficiency*. Presented at: 27th International Technical Conference on Coal Utilization and Fuel Systems. Clearwater, Fl: CTA, 2002:719–729.
8. de Diego LF, Gayan P, Garcia-Labiano F, Celaya J, Abad A, Adanez J. Impregnated CuO/Al_2O_3 oxygen carriers for chemical-looping combustion: avoiding fluidized bed agglomeration. *Energy Fuels*. 2005;19:1850–1856.
9. Ishida M, Jin H. A new advanced power-generation system using chemical-looping combustion. *Energy*. 1994;19:415–422.
10. Lingfelt A, Leckner B, Mattison T. A fluidized-bed combustion process with inherent CO_2 separation; application of chemical-looping combustion. *Chem. Eng. Sci.* 2001;56:3101–3113.
11. Ryden M, Lyngfelt A, Mathisson T. Synthesis gas generation by chemical-looping reforming in a continously operating laboratory reactor. *Fuel*. 2006;85:1631–1641.
12. Adanez J, Garcia-Labiano F, de Diego LF, Gayan P, Celaya J, Abad A, Nickel-copper oxygen carriers to reach zero CO and H2 emmissions in chemical-looping combustion. *Ind. Eng. Chem. Res.* 2006;45:2617–2625.
13. Dewaele O, Froment GF. TAP study of the mechanism and kinetics of the adsorption and combustion of methane on Ni/Al_2O_3 and NiO/Al_2O_3. *J Catal*. 1999;184:499–513.
14. Xu J, Froment GF. Methane steam reforming, methanation and water-gas shift: I. Intrinsic kinetics. *AIChE J*. 1989;35:88–96.
15. Szekely J, Evans JW, Sohn HY. *Gas-solid reactions*. New York: Academic Press, 1976.
16. Heesink ABM, Prins W, Swaaij WPM. A grain size distribution model for non-catalytic gas-solid reactions. *Chem Eng J*. 1993;53:25–37.
17. Bhatia SK, Perlmutter DD. A random pore model for fluid-solid reactions, I. Isothermal, kinetic control. *AIChE J*. 1980;26:379–386.
18. Bhatia SK, Perlmutter DD. A random pore model for fluid-solid reactions, II. Diffusion and transport effects. *AIChE J*. 1981;27:247–254.
19. Gavalas GR. A random capillary model with application to char gasification at chemically controlled rates. *AIChE J*. 1980;26:577–585.
20. Gavalas GR. Analysis of char combustion including the effect pore enlargement. *Combust Sci Technol*. 1981;24:192–197.
21. Son SR, Kim SD. Chemical-looping combustion with NiO and Fe_2O_3 in a thermobalance and circulating fluidized bed reactor with double loops. *Ind Eng Chem Res*. 2006;45:2689–2696.
22. Gomez-Barea A, Ollero P. An approximate method for solving gas-solid non-catalytic reactions. *Chem Eng Sci*. 2006;61:3725–3735.
23. Hou K, Houghes R. The kinetics of methane reforming over a Ni/α-Al_2O_3 catalyst. *Chem Eng J*. 2001;82:311–328.
24. Wang S, Lu GQM. A comprehensive study on carbon dioxide reforming of methane over Ni/γ-Al_2O_3 catalysts. *Ind Eng Chem Res*. 1999;38:2615–2625.
25. Klose J, Baerns M. Kinetics of the methanation of carbon monoxide on an aluminja-supported nickel catalyst. *J Catal*. 1984;85:105–116.

26. Cho P, Mattisson T, Lyngfelt A. Carbon formation on nickel and iron oxide-containing oxygen carriers for chemical-looping combustion. *Ind Eng Chem Res*. 2005;44:668–676.
27. Snoeck JW, Froment GF, Fowles M. Kinetic study of the carbon filament formation by methane cracking on a nickel catalyst. *J Catal*. 1997;169:250–262.
28. Snoeck JW, Froment GF, Fowles M. Steam/CO_2 reforming of methane. Carbon filament formationj by the Boudouard reaction and gasification by CO_2, by H_2, and by steam: kinetic study. *Ind Eng Chem Res*. 2002;41:4252–4265.
29. Froment GF, Bischoff KB. *Chemical reactor analysis and design*. New York: Wiley, 1990.
30. Sicardi S, Baldi G, Specchia V. Hydrodynamic models for the interpretation of the liquid flow in trickle-bed reactors. *Chem Eng Sci*. 1980;35:1775–1782.
31. Kunii D, Levenspiel O. Bubbling bed model. *Ind Eng Chem Fund*. 1968;7:446–452.
32. Davidson JF, Harrison D. *Fluidizations Particles*. New York: Cambridge University Press, 1963.
33. Gascon J, Tellez C, Herrguido J, Jakobsen HA, Menendez M. Modeling of fluidized bed reactors with two reaction zones. *AIChE J*. 2006;52:3911–3923.
34. Hoffmann Ac, Janssen LPBM, Prins J. Particle segregation in fluidized binary-mixture. *Chem Eng Sci*. 1993;48:1583–1592.
35. Naimer NS, Chiba T, Nienow A. Parametric estimation for solids mixing/segregation model for gas fluidized beds. *Chem Eng Sci*. 1982;37:1047–1057.
36. Sane SU, Haynes HW, Agarwal PK. An experimental modelling investigation of gas mixing in bubbling fluidized beds. *Chem Eng Sci*. 1996;51:1133–1147.
37. Zafar Q, Abad A, Mattisson T, Gevert B. Reaction kinetics of freeze-granulated NiO/$MgAl_2O_4$ oxygen carrier particles for chemical-looping combustion. *Energy Fuels*. 2007;21:610–618.
38. Mattisson T, Garcia-Labiano F, Kronberger B, Lyngfelt A, Adanez J, Hofbauer H. Chemical-looping combustion using syngas as fuel. *Int J Greenhouse Gas Control*. 2007;1:158–169.
39. Abad A, Adanez J, Garcia-Labiano F, de Diego LF, Gayan P, Celaya J. Mapping of the range of operational conditions for Cu-, Fe-, and Ni-based oxygen carriers in chemical-looping combustion. *Chem Eng Sci*. 2007;62:533–549.
40. Ishida M, Jin H, Okamoto T. A fundamental study of a new kind of medium material for chemical-looping combustion. *Energy Fuels*. 1996;10:958–963.
41. Corbella BM, de Diego LF, Garcia-Labiano F, Adanez J, Palacios JM. Performance in a fixed-bed reactor of titania-supported nickel oxide as oxygen carriers for chemical-looping combustion of methane in multicycle tests. *Energy Fuels*. 2005;19:433–441.
42. Claridge JB, Green MLH, Tsang SC, York AP, Ashcroft AT, Battle PD. A study of carbon deposition on catalyst during partial oxidation of methane to synthesis gas. *Catal Lett*. 1993;22:299–304.
43. Jin H, Okamoto T, Ishida M. Development of a novel chemical-looping combustion: synthesis of a solid looping material of NiO/$NiAl_2O_4$. *Ind Eng Chem Res*. 1999;38:126–132.
44. Lippens BC, Mulder J. Prediction of the minimum fluidization velocity. *Powder Technol*. 1993;75:67–78.
45. Darton RC, La Nauze RD, Davidson JF, Harrison D. Bubble growth due to coalescence in fluidized beds. *Trans Inst Chem Eng*. 1977;55:274–280.
46. Horio M, Nonaka A. A generalized bubble diameter correlation for gas-solid fluidized beds. *AIChE J*. 1987;33:1865–1872.
47. Lim KS, Gururajan VS, Agarwal PK. Mixing of homogeneous solids in bubbling fluidized beds: theoretical modelling and experimental investigation using digital image analysis. *Chem Eng Sci*. 1993;48:2251–2265.

Manuscript received Nov. 12, 2008, and revision received May 5, 2009.